Naval Surface Warfare Center
Carderock Division
West Bethesda, MD 20817-5700

NSWCCD-65-TR–2020/07 December 2020

Platform Integrity Department

Technical Report

Validation of Ductile Metal Rupture/Tearing Material Models for Simulation of Structure/Ice Collision Events

by

Douglas E. Lesar

NSWCCD-65-TR–2020/07 Validation of Ductile Metal Rupture/Tearing Material Models for Simulation of Structure/Ice Collision Events

Naval Surface Warfare Center
Carderock Division
West Bethesda, MD 20817-5700

NSWCCD-65-TR–2020/07 December 2020
Platform Integrity Department Technical Report

Validation of Ductile Metal Rupture/Tearing Material Models for Simulation of Structure/Ice Collision Events

by

Douglas E. Lesar

REPORT DOCUMENTATION PAGE

Form Approved
OMB No. 0704-0188

1. REPORT DATE *(DD-MM-YYYY)*	2. REPORT TYPE	3. DATES COVERED *(From - To)*
02-Dec-2020	Final	-

4. TITLE AND SUBTITLE

Validation of Ductile Metal Rupture/Tearing Material Models for Simulation of Structure/Ice Collision Events

5a. CONTRACT NUMBER
N0001420WX0113799

5b. GRANT NUMBER

5c. PROGRAM ELEMENT NUMBER
0602123N

6. AUTHOR(S)

Douglas E. Lesar

5d. PROJECT NUMBER

5e. TASK NUMBER

5f. WORK UNIT NUMBER

7. PERFORMING ORGANIZATION NAME(S) AND ADDRESS(ES) AND ADDRESS(ES)

Naval Surface Warfare Center
Carderock Division
9500 Macarthur Boulevard
West Bethesda, MD 20817-5700

8. PERFORMING ORGANIZATION REPORT NUMBER

NSWCCD-65-TR–2020/07

9. SPONSORING / MONITORING AGENCY NAME(S) AND ADDRESS(ES)

Attn: ONR 331
Chief of Naval Research
One Liberty Center
875 N. Randolph Street,
Suite 1425
Arlington, VA 22203-1995

10. SPONSOR/MONITOR'S ACRONYM(S)

11. SPONSOR/MONITOR'S REPORT NUMBER(S)

12. DISTRIBUTION / AVAILABILITY STATEMENT

Distribution Statement A. Approved for public release. Distribution is unlimited.

13. SUPPLEMENTARY NOTES

14. ABSTRACT

This report documents validation of numerical methods for simulation of rupture and tearing damage inflicted on indenter-loaded thin shell structures. These modeling methods are key to accurate prediction of ice impact loads and resulting structural damage that risk the hull structural integrity of non-ice-reinforced naval surface ships transiting ice-infested waters. Validation is accomplished by successful numerical-mechanics simulation of laboratory experiments. Steel structure rupture and tearing simulations are carried out for three flat panels, all loaded by conically-profiled rigid indenters driven laterally into the panels at effectively static rates until rupture occurs. An unstiffened panel and panels reinforced with one and two flat bar stiffeners are considered, all supported in a rigid box-sided frame. The stress-strain behavior of the steels in all plate and stiffener components is characterized to enable representation of failure strain levels as a function of stress triaxiality through a forming limit diagram approach. This same approach had been used in a prior series of exploratory analyses of notional ship hull structure severely damaged by indenters driven over the hull structure in a "raking" fashion. The present numerical simulations produce structural displacement, failure load, and fracture pattern results consistent with the laboratory experiments and comparable to those of previous researchers. A moderate degree of mesh sensitivity of predicted failure loads and fracture patterns is observed, especially in the case of the panel reinforced by two stiffeners, for which fracture initiation sites are in zones of extreme strain gradient.

15. SUBJECT TERMS

Ship Structures, Structural Damage, Structural Failure Modes, Finite Element Analysis

16. SECURITY CLASSIFICATION OF:			17. LIMITATION OF ABSTRACT	18. NUMBER OF PAGES	19a. NAME OF RESPONSIBLE PERSON
a. REPORT	b. ABSTRACT	c. THIS PAGE			Mr. Douglas E. Lesar
UNCLASSIFIED	UNCLASSIFIED	UNCLASSIFIED	SAR	68	19b. TELEPHONE NUMBER *(include area code)* (301)227-1803

This page intentionally left blank.

Contents

Page

Figures

Page

Tables

Page

Preface

The Structures and Composites Division (Code 65) of the Platform Integrity Department at Naval Surface Warfare Center, Carderock Division (NSWCCD) performed the work described in this report during the period from October 2019 to July 2020. Office of Naval Research (ONR), Sea Warfare and Weapons Department, Ship Systems and Engineering Research Division (ONR 331) provided funding to support this effort. NSWCCD performed the work under funding documents N0001419WX00399, N0001420WX00583, N0001420WX01096, and N0001420WX01137, program element 0602123N.

ONR requested NSWCCD to develop capabilities, using advanced computational structural dynamics modeling and simulation (M&S) methods, for simulation of response and failure analysis of non-ice-classed ship structures subjected to collision with sea ice in the marginal ice zone. Two motivations impel this work: (1) a need to advance U.S. Navy's (USN) ability to quantify the risk associated with operating surface combatants in ice-infested polar waters, and (2) a need to develop surface combatant operating guidance minimizing risk to hull structural integrity during polar-region operations. This document is a continuation of a prior NSWCCD report (Lesar, 2020), which documents structure and ice collision simulations considering rupture and tearing damage in the structure as a function of ice crushing compliance. This report concerns experimental validation of simulation methods for structural rupture and tearing damage.

Acknowledgments

The author thanks Dr. Paul Hess III of ONR for, starting in 2010, having the foresight to restore USN science and technology (S&T) attention to this increasingly important technical area. Thanks are also extended to Dr. Ken Nahshon (NSWCCD 664), who provided key advice and guidance concerning cost-effective and engineering-level accurate numerical modeling of fracture and tearing behaviors in thin shell structures. The hardware and software resources of the Department of Defense (DoD) High Performance Computing Centers were essential to timely completion of the dozens of simulations performed in the course of this effort.

1. Summary

This report documents validation of numerical methods for simulation of rupture and tearing damage inflicted on indenter-loaded thin shell structures. These modeling methods are key to accurate prediction of ice impact loads and resulting structural damage that risk the hull structural integrity of non-ice-reinforced naval surface ships transiting ice-infested waters. Validation is accomplished by successful numerical-mechanics simulation of laboratory experiments.

Steel structure rupture and tearing simulations are carried out for three flat panels, all loaded by conically-profiled rigid indenters driven laterally into the panels at effectively static rates until rupture occurs. An unstiffened panel and panels reinforced with one and two flat bar stiffeners are considered, all supported in a rigid box-sided frame. The stress-strain behavior of the steels in all plate and stiffener components is characterized to enable representation of failure strain levels as a function of stress triaxiality through a forming limit diagram (FLD) approach. This same approach had been used in a prior series of exploratory analyses of notional ship hull structure severely damaged by indenters driven over the hull structure in a “raking” fashion. The present numerical simulations produce structural displacement, failure load, and fracture pattern results consistent with the laboratory experiments and comparable to those of previous researchers. A moderate degree of mesh sensitivity of predicted failure loads and fracture patterns is observed, especially in the case of the panel reinforced by two stiffeners, for which fracture initiation sites are in zones of extreme strain gradient.

2. Introduction

Existing semiempirical toolsets are adequate for design and assessment of ice-classed hull structures for ships that are completely dedicated to icebreaking or must routinely operate in ice-infested waters. However, these toolsets assume robust hull structural configurations incompatible with currently-dominant structural weight-optimized warship hull structure designs. Ice-classed hull structural configurations would also pose arrangement and cost challenges when applied to warships. This report focuses on numerical modeling and simulation (M&S) methods accounting for large hull structure deformation, plasticity, tearing, and rupture to investigate the shared-energy collision and damage physics phenomena that are likely present when non-ice-classed hull structure collides with floe or glacial ice.

Previous ship structure/ice impact simulation studies by Lesar (2017, 2019), using the LS-DYNA explicit nonlinear dynamics analysis code (Livermore Software Technology Corporation (LSTC, 2017)), focused on thin-ice impact scenarios where loading, limited by low relative ice/structure velocity and low ice body mass and stiffness, confines structural damage to permanent set deformation short of structural rupture and tearing. In some high latitude waters, impact by difficult-to-detect glacial ice pieces of sizes approaching or exceeding ship mass ("bergy bits") may be a more hazardous scenario. Another LS-DYNA simulation study, using the same notional ship structure idealization employed in Lesar (2019), considered indentation and "raking" loading by both rigid indenters and compliant indenters idealized with material models approximating large-scale ice crushing (Lesar, 2020). This work extended an earlier exercise (Dolny, Daley, Quinton, & Daley, 2017), allowing occurrence (in addition to permanent set) of structural rupture and tearing damage through use of a forming limit diagram (FLD) approach. These simulations reinforced the observations of Dolny et al. (2017, section 3.4) that traveling loads induce greater structural damage than stationary loadings, and showed a dependence of rupture and tearing damage occurrence and extent on indenter compliance. The performance of the FLD approach for assessing severely damaging ship structure ice impact is encouraging, but experimental validation is needed before this methodology can be incorporated into large-scale numerical analyses informing design assessment and/or operational risk avoidance guidance.

This report addresses the validation of a FLD approach for thin plate fracture initiation and propagation. This is accomplished by LS-DYNA simulations of structural panel punch tests, wherein smooth rigid indenters are slowly pushed into rigidly supported unstiffened and stiffened steel plates until rupture and tearing occurs. These tests, conducted by NTNU (Technical University of Norway, Trondheim), are documented in Alsos and Amdahl (2009), and NTNU-performed numerical simulations of these tests are documented in Alsos, Amdahl, and Hopperstad (2009). In the present effort, a FLD approach that requires minimal stress vs. strain data and is readily applied in the LS-DYNA code is used, and the specified meshes are practical to consider in analyses involving large extents of ship structure. Although the NTNU tests employ rigid indenters instead of ice bodies, these tests provide a well-documented data set for validation of practical ship structure modeling methods for the ship/ice impact problem.

This work is carried out via the modeling methods and assumptions delineated in section 3. The results of these simulations and findings are detailed in section 4; overall summaries are listed in the conclusion detailed in section 5, and section 6 provides recommendations for future work in this challenging area.

3. Methods, Assumptions, and Procedures

This major section describes the test specimens analyzed, their numerical discretizations and material modeling assumptions, the modeled indenters, kinematic assumptions of the structure and indenter interaction, and numerical modeling software and computation hardware.

3.1 Analysis Software

LS-DYNA is a general-purpose, three-dimensional (3D), nonlinear finite element analysis (FEA) code, developed and maintained by LSTC (2017). This code addresses high-rate dynamic problems in which large deflections, complex evolving mechanical contacts, nonlinear material behavior, and material failure are predominant. It addresses static and dynamic problems involving solids and structures, possesses adjunct fluid domain modeling capabilities, and enables treatment of various fluid-structure interactions. It uses explicit time-integration methods, but it can also carry out implicit solution of low-rate or static problems. Several LS-DYNA applications to problems in the ice mechanics and ice/structure impact areas may be cited (Das, Polić, Ehlers, & Amdahl, 2014; Gagnon & Derradji-Aouet, 2006; Gagnon & Wang, 2012; Kim, 2014; Kim et al., 2016; Liu, Amdahl, & Løset, 2011; Sazidy, 2015).

The next section describes the quasi-static unstiffened and stiffened panel punch tests conducted by NTNU.

3.2 Laboratory Experiments

The conduct and results of the NTNU-executed rupture experiments on five unstiffened and stiffened panels are documented in Alsos and Amdahl (2009). A rigid smooth-profiled punch quasi-statically loaded the panels transversely until the panels ruptured. Table 1 lists the panel configurations that included flat-bar and bulb stiffeners.

Table 1. NTNU Punch Test Specimen Configurations

Specimen ID	Number of Stiffeners	Stiffener Type
US	None	-
1-FB	One	Flat Bar
2-FB	Two	Flat Bar
1-HB	One	Bulb
2-HB	Two	Bulb

The test articles, their stiff and massive box frame edge supports, and their major lateral dimensions and thicknesses in millimeter units are pictured in Figure 1. Inclusion of singly- and doubly-stiffened panels in the test series allowed consideration of loading between stiffeners and on a stiffener. The flat plates of all panels have the same thickness and lateral dimensions. The unstiffened panel and the two flat bar-stiffened panels were considered as subjects for LS-DYNA simulation. Although the bulb-stiffened panels demonstrated unique response characteristics, these were judged to be secondary to the purposes of this effort and are not considered.

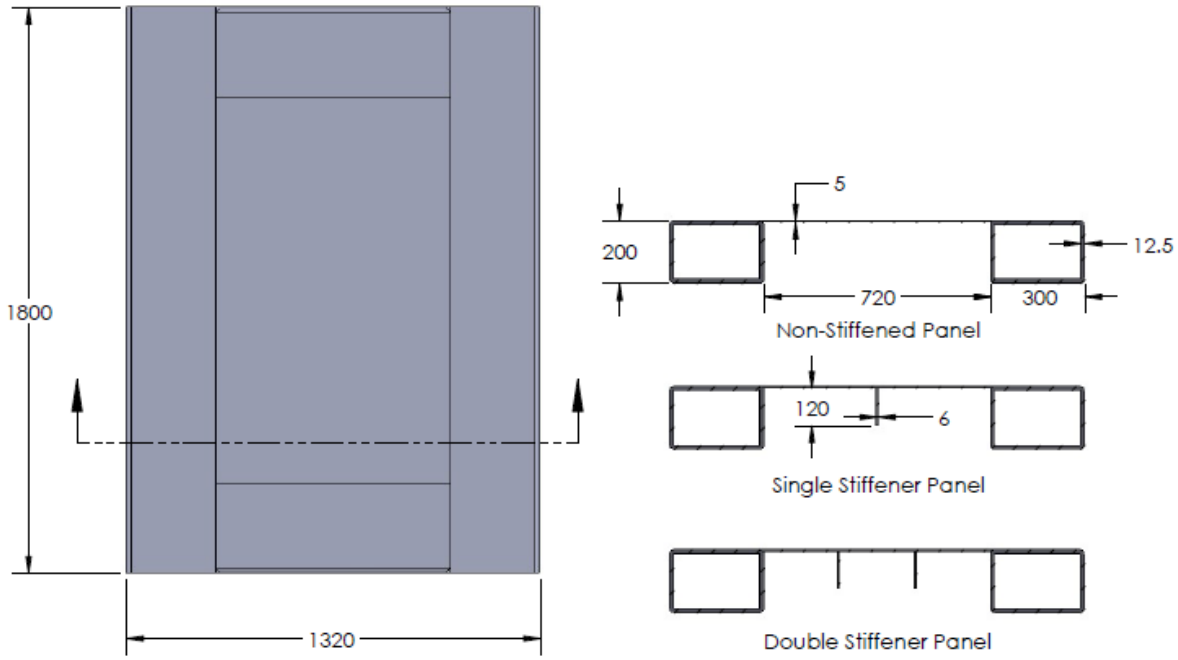

(a) Plan View **(b) Section Views**

Figure 1. NTNU Rupture Test Specimens. Adapted from "On the Resistance to Penetration of Stiffened Plates, Part I: Experiments," by H. S. Alsos and J. Amdahl, 2009, *International Journal of Impact Engineering*, 36, p. 801.

NTNU acquired engineering stress-strain curves for material characterization specimens oriented with, and perpendicular to, the thin sheet steel rolling direction. NTNU published "average" curves since property differences for the two directions were not significant. The flat plates and flat bars are "mild steel" (grade S235JR EN10025) and the supporting boxes are "high strength steel" (grade S355NH EN10210). The mild steel flat bar demonstrated higher strength than the mild steel plate, probably due to production batch property differences. The graphical presentations of measured stress-strain curves in Alsos and Amdahl (2009) were digitized, and their representation in LS-DYNA models is described in section 3.3.2.

Figure 2 illustrates the punch testing configuration, showing the hydraulic jack, the jack and specimen support frame, the jack-driven indenter, the boxes reinforcing the specimen edges, and a typical test specimen. The indenter is milled from a solid steel block and has a conical profile with a spherical nose. The spreading angle of the cone is 90 degrees and the nose radius is 200 mm.

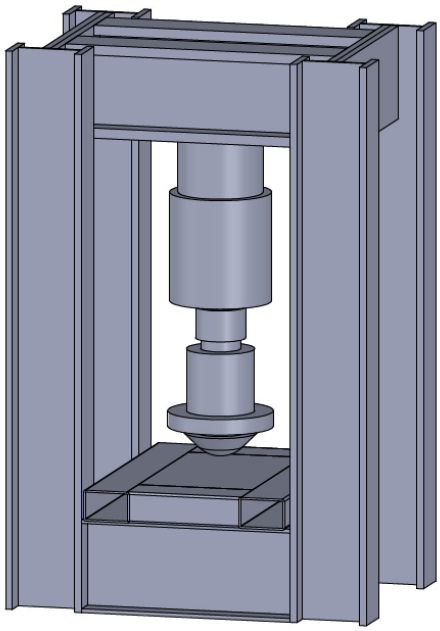

Figure 2. NTNU Rupture Test Specimen with Loading Frame and Rigid Indenter. Adapted from "On the Resistance to Penetration of Stiffened Plates, Part I: Experiments," by H. S. Alsos and J. Amdahl, 2009, *International Journal of Impact Engineering*, 36, p. 802.

Hydraulic jack loading is displacement-controlled, at a vertical movement rate of 10 mm/min (1m/6000s). Indenter force and displacement are measured on the jack crosshead, and "rig stretch" is accounted for by independent measurement of indenter displacement relative to ground. These measurements allowed development of force vs. indentation curves, which are presented in Alsos and Amdahl (2009). Photographs of specimen state were taken at 5-second intervals. The specimens were not instrumented, though 100 x 100 mm grids drawn on the plate surfaces aided in visualizing deformations. These investigators also estimated dissipated fracture energies for each specimen and examined crack patterns and fracture surfaces for failure mechanism clues.

The next section documents assumptions and modeling methods used in LS-DYNA simulations of the NTNU laboratory tests.

3.3 Simulation Modeling

LS-DYNA idealizations of the NTNU test specimens embraced the same discretization techniques (thin shell modeling for specimens and rigid body modeling of indenter), load history representation, and test article displacement and rotation boundary conditions employed in the NTNU LS-DYNA simulations. However, steel material property definitions and FE model shell element mesh density followed different motivations and methodologies. These two considerations are related, but discussion first focuses on material property assumptions.

3.3.1 Material Properties

In addition to accomplishing experiments, the NTNU investigators sought to validate FE-based methods for modeling fracture and failure of large but intensely-locally-loaded stiffened plate (ship) structures; their efforts appear in Alsos, Amdahl, and Hopperstad (2009). In LS-DYNA simulations of their five punch tests, NTNU considered two tensile failure criteria for

ductile metals based on material instability ("necking") in the vicinity of ultimate tensile stress. These are (1) RTCL; see Rice and Tracey (1969) and Cockcroft and Latham (1968), and (2) BWH; see Bressan and Williams (1983) and Hill (1952)[1]. Both of these criteria can be considered as "forming limit diagram" (FLD) methods, in which effective (inelastic) failure strains are defined as a function of multidimensional stress state, particularly considering the presence of hydrostatic stress. Despite the simplifications of failure process modeling via FLD equations particular to two-dimensional stress states assumed to prevail in thin plates, their simulations credibly reproduced their test specimen's measured load vs. displacement data and provided reasonable calculated test specimen tearing patterns at failure. Notably, however, predictions based on the RTCL criterion were considerably more mesh-dependent than for the BWH criterion.

An additional two-dimensional FLD theory (HSR; see Hill (1952) and Stören and Rice (1975)) is particularly easy to develop from uniaxial tensile stress-strain test data. An LS-DYNA ship structure/ice impact M&S study considering rupture and tearing damage in the structure (Lesar, 2020) utilized this method to define stress triaxiality-dependent failure criteria for the collision-loaded ship structure. This effort seeks to validate this failure criterion choice under the constraint of practical thin shell FE mesh density.

Development of a stress triaxiality-dependent failure strain curve follows from uniaxial tensile test specimen data. The NTNU-reported engineering stress vs. engineering strain curves for mild steel specimens for both the flat plate and the flat bar stiffeners, plus parallel data for the high strength steel support boxes (see Figure 3 of Alsos & Amdahl, 2009), was digitized and converted to true stress vs. true strain curves defined up to measured ultimate stress. Power law curve-fitting of this data provided the coefficients needed to calculate effective failure strain vs. stress triaxiality curves according to the HSR approach. The following discussion focuses only on inputs and results of this process. Further process details, carried out for DH36 steel, are provided in Lesar (2020).

Table 2 lists the basic material properties, in both Imperial and MKS units, of the NTNU specimen steels relevant to the unstiffened and flat- bar-stiffened panels. Note the difference between plating and flat bar yield strengths, even though both satisfied minimum mild steel strength requirements. In this table and subsequently, the acronym "MS" denotes mild steel, and "HSS" denotes high strength steel.

[1] Section 2.2 of Alsos, Amdahl, and Hopperstad (2009) provides practical engineering justification for the use of necking onset as a failure criterion in place of fracture initiation, which requires a significant burden on numerical modeling of large built-up structures. Basing failure load prediction on necking onset is likely to be conservative relative to the load causing fracture.

Table 2. NTNU Specimen Steel Material Properties

Material Property, All Steels	Value in U.S. (Imperial) Units	Value in SI (MKS) Units
Mass Density	0.284 lbf/in^3	7850 kg/m^3
Elastic Modulus	29.6 Msi	204 GPa
Poisson's Ratio	0.3	0.3
Plating MS (S235JR EN10025)		
Yield Strength	41.4 ksi	285 MPa
Flat Bar MS (S235JR EN10025)		
Yield Strength	49.3 ksi	340 MPa
Support Box HSS (S355NH EN10210)		
Yield Strength	56.6 ksi	390 MPa

The LS-DYNA material model used is MAT_TABULATED_JOHNSON_COOK (MAT224). Xue (2007) presents the underlying theory of the model, and Xue and Wierzbicki (2006) mention LS-DYNA implementation of the model. MAT224 is an elastic-viscoplastic material model that accepts arbitrary piecewise linear stress-strain curves and arbitrary strain-rate dependency. This effort does not need the model's capability for accounting for material softening by plastic heating. Failure through element deletion ("fracture") may be triggered at specified effective strain levels monitored at element integration points, with optional failure-strain dependencies on stress triaxiality, strain rate, temperature, and/or element size. Temperature dependence is not a present concern, and, as discussed previously, strain rate effects are judged to be minor for the loading rates of the NTNU tests. On-the-fly failure-strain calibration according to element size can compensate for fracture-prediction mesh sensitivity. However, optimal structural FE model meshing can avoid the need for element-size correction functions. This issue is addressed in later discussion.

Figure 3 contains graphs of the digitized NTNU-measured engineering stress-engineering strain data for the three steel types, converted to true stress vs. true strain. The sampling points were adjusted slightly to provide well-behaved curves for LS-DYNA yield stress vs. effective plastic strain input (labelled "smoothed LS-DYNA input"), and points lying beyond ultimate stress were discarded (labelled "discarded points"). Figure 3 also shows power law curvefits that are valid for the data in the effective plastic strain range from 0.1 to 0.3. The coefficients of these fits (K and N) are needed to develop the HSR theory-based effective failure strain curves. The coefficient N is particularly important, as $2N/\sqrt{3}$ is the minimum effective failure strain value under conditions of plane strain tension.

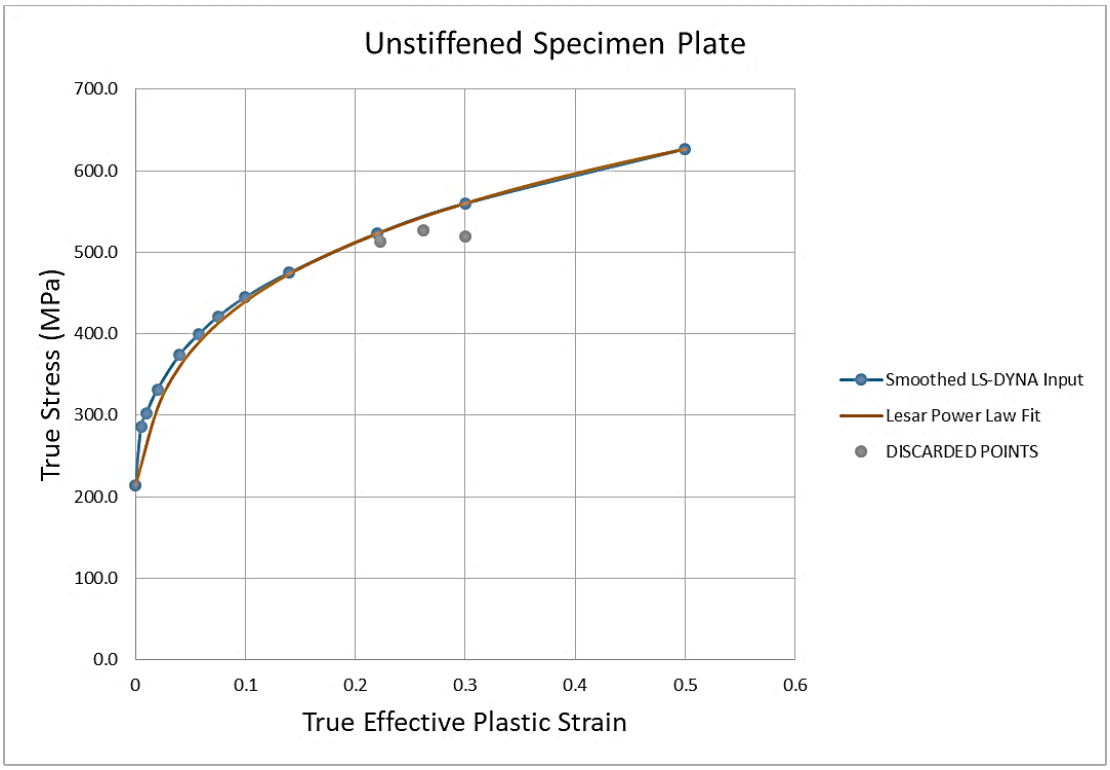

(a) Mild Steel Plating

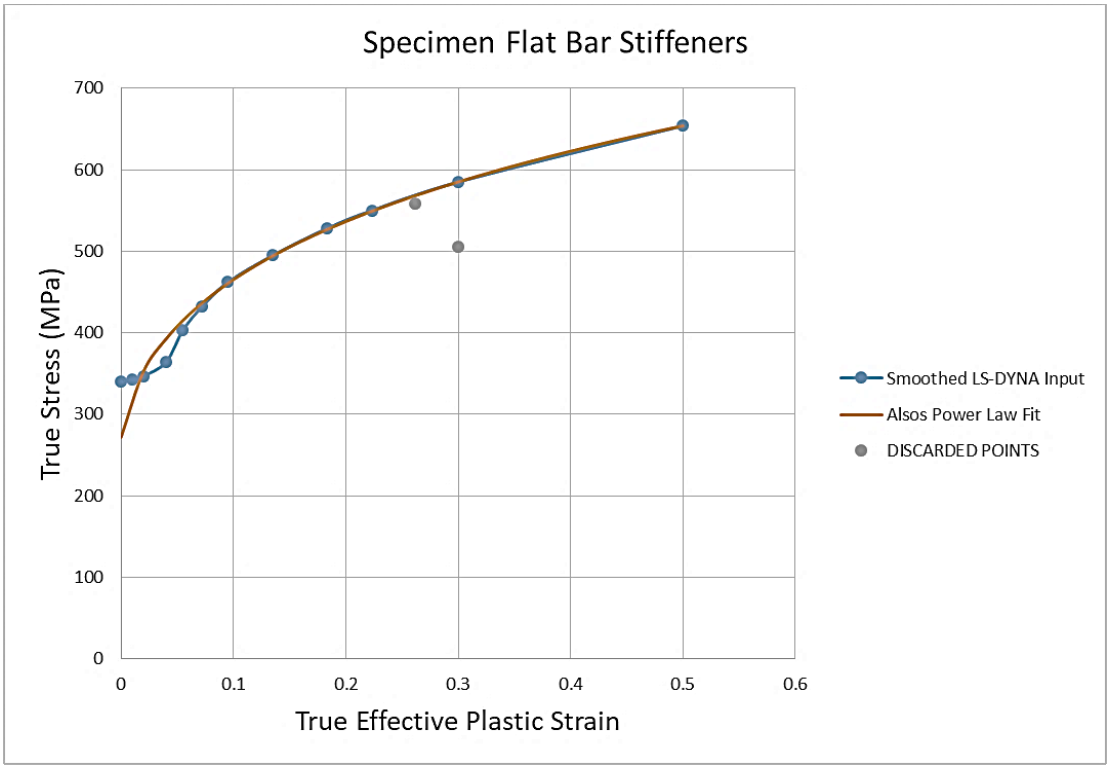

(b) Mild Steel Flat Bars

Figure 3. True-Stress-versus-True-Strain Curves for NTNU Test Specimen Steels

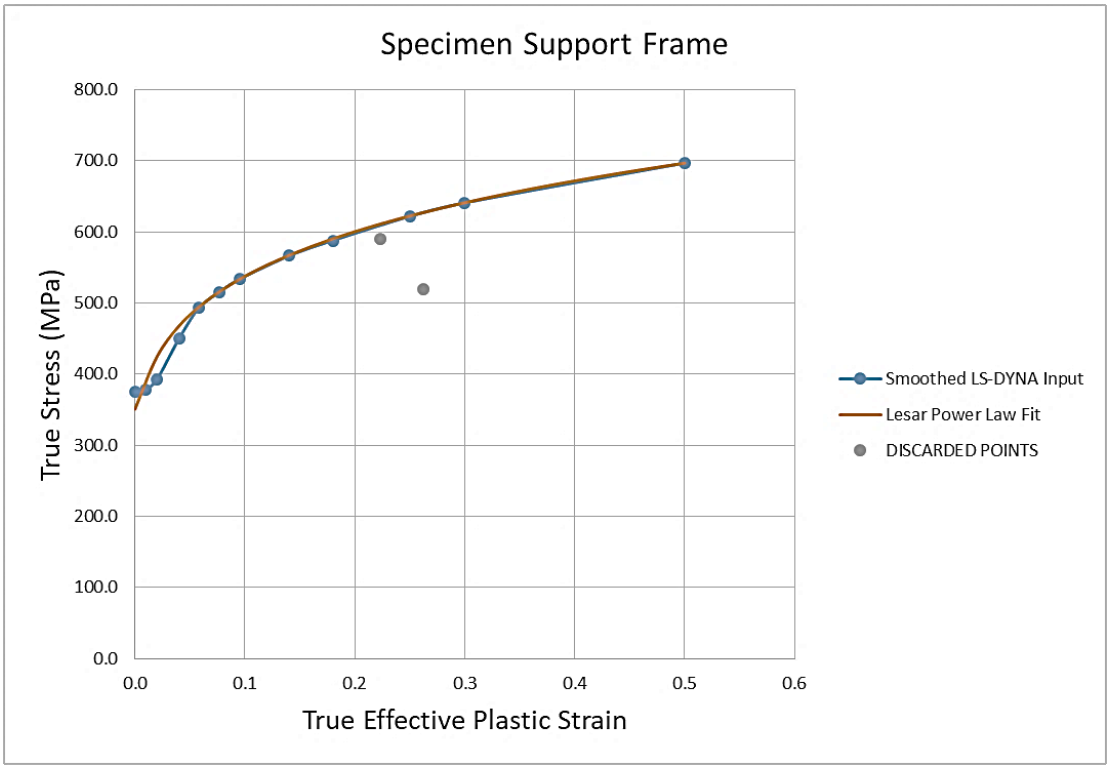

(c) High Strength Steel Support Boxes

Figure 3. True-Stress-versus-True-Strain Curves for NTNU Test Specimen Steels (cont'd)

NTNU did not document their entire process for generating stress-strain curves for their LS-DYNA simulations, but they did publish their derived power law coefficients K and N (see Table 2 of Alsos, Amdahl and Hopperstad, 2009). At the same time, the data fits performed for this NSWCCD effort produced slightly different coefficients for two of the three materials. These are compared in Table 3.

Table 3. NTNU- and NSWCCD-Derived Power Law Coefficients for NTNU Specimen Steels

Specimen Component	Steel Type	NTNU		NSWCCD	
		K (MPa)	N	K (MPa)	N
Plating	MS	740	0.24	730	0.22
Flat Bar	MS	760	0.225	760	0.225
Support Box	HSS	830	0.18	780	0.165

The greatest difference between NTNU and NSWCCD coefficients is for the high strength steel, but this result is inconsequential as the support box is not loaded anywhere close to failure. The NTNU coefficients for the flat bar steel are found to be accurate. There is a possibility that the N = 0.24 coefficient for the plating steel may have been erroneously switched in the NTNU property data table with N = 0.22 for one of the bulb-stiffened specimens.

Table 4, Table 5, and Table 6 provide the LS-DYNA input coordinates of the piecewise linear effective-plastic (true)-strain curves for the three NTNU test specimen steels as a function of effective (true) stress.

Table 4. True-Stress-versus-Effective Plastic Strain for NTNU Test Specimen Plating Steel

Effective Plastic Strain	Effective True Stress (MPa)
0.0	214
0.005	286
0.010	303
0.020	332
0.040	374
0.058	400
0.075	421
0.100	445
0.140	475
0.182	495
0.220	523
0.300	560
0.500	627

Table 5. True-Stress-versus-Effective Plastic Strain for NTNU Test Specimen Flat Bar Steel

Effective Plastic Strain	Effective True Stress (MPa)
0.0	340
0.010	343
0.020	347
0.040	364
0.055	403
0.072	432
0.095	462
0.135	495
0.183	528
0.223	550
0.300	585
0.500	654

Table 6. True-Stress-versus-Effective Plastic Strain for NTNU Test Specimen Support Box Steel

Effective Plastic Strain	Effective True Stress (MPa)
0.0	375
0.010	379
0.020	393
0.040	450
0.058	493
0.077	516
0.095	534
0.140	566
0.180	588
0.250	622
0.300	641
0.500	697

Appendix A of Lesar (2020) documents development of the DH36 steel failure-strain curve for plane-stress conditions, using the HSR FLD construction method based on the hardening parameter N. (This appendix is reproduced as the Appendix of this report with a new reference to additional DH36 property measurements that the author was unaware of when the original Appendix was developed). Table 7 contains similar results for the three NTNU specimen steel types, using the NSWCCD-derived N parameters given in Table 3. Failure strains are presented as a function of stress triaxiality, *T*, (ratio of mean stress or pressure to effective stress) defined over the range from $-2/3$ to roughly zero[2]. This range covers conditions of biaxial tension ($T = -2/3$), plane-strain tension ($T = -1/\sqrt{3}$, or –0.577), and uniaxial tension ($T = -1/3$). Although the curves extend to shear-dominated stress triaxiality ($T \rightarrow 0$), they become nonconservative and overestimate failure strain as $T < -1/3$. Inaccurate triaxiality dependence in these shear-dominated stress states is acceptable in FE analysis with thin-shell elements under the tacit assumption of plane-stress conditions. Confinement to plane-stress conditions also obviates the need to account for failure-strain dependence on Lode Angle, an additional stress state invariant that is necessary for full 3D stress-state characterization. The data in Table 7 indicates slightly greater margin against failure in the MS flat bar stiffeners versus the MS plating, and distinctly lower failure strain levels in the less ductile HSS support structure.

[2] The negative sign convention for triaxiality is unusual compared to most papers in the literature. Apparently, the negative-sign convention was followed when MAT224 was originally developed as a user-defined material. Also apparently, insertion of this user-defined material into LS-DYNA left this convention intact, and the main code performs triaxiality algebraic sign adjustment to conventional form prior to output delivery for post-processing.

Table 7. Failure Strains as a Function of Stress Triaxiality for NTNU Specimen Steels

Stress Triaxiality	Effective Failure Strain		
	MS in Plating	MS in Flat Bars	HSS in Support Boxes
-0.667	0.553	0.558	0.498
-0.666	0.518	0.523	0.462
-0.665	0.481	0.486	0.424
-0.663	0.444	0.449	0.383
-0.660	0.407	0.413	0.348
-0.655	0.371	0.376	0.311
-0.647	0.337	0.342	0.276
-0.637	0.305	0.311	0.243
-0.622	0.279	0.285	0.216
-0.603	0.261	0.267	0.198
-0.577	0.254	0.260	0.191
-0.545	0.269	0.275	0.202
-0.504	0.291	0.298	0.218
-0.455	0.323	0.330	0.242
-0.397	0.369	0.377	0.277
-0.333	0.440	0.450	0.330
-0.265	0.554	0.566	0.415
-0.195	0.753	0.770	0.565
-0.126	1.164	1.191	0.873
-0.0605	2.423	2.478	1.817

The data listed in Table 7 is graphed in Figure 4, with the sign of triaxiality reversed to more conventional positive values. The difference in failure strains between specimen plating and the flat bar stiffeners is slight and barely visible at the given plot scaling. However, the lower support box material ductility is evident.

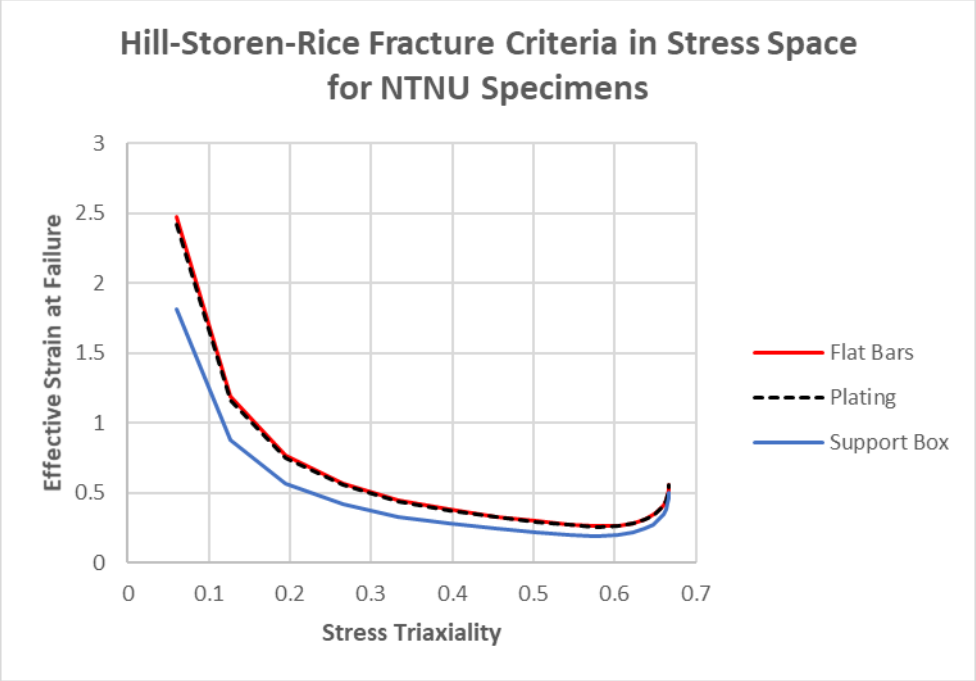

Figure 4. Failure Strains versus Stress Triaxiality for NTNU Specimen Components

The MAT224 parameter *numint*, the number of element integration points that must reach failure conditions before an element is deleted, is specified as five, the number of evenly-spaced through-thickness integration points in all shell elements in the NTNU specimen FEMs. This stringent element deletion criterion prevented runaway shattering behavior and brought about physically reasonable crack patterns when modeling fracture of brittle ice slabs (Lesar (2017) and Lesar (2019)). It is possible that this assumption is overly conservative for ductile materials like NTNU specimen steels, but relaxing *numint* to less than the total number of element integration points was not investigated in this study.

The binary 0 or 1 choice of the parameter *failopt* governs the load-path (and time) dependency of how failure conditions are reached. *Failopt* = 0 (default) triggers load-path dependence, wherein failure occurs when the time integral of effective strain increments reaches failure strain. *Failopt* = 1 invokes load-path independence, wherein failure occurs when the current state of effective plastic strain reaches failure strain. As there is no guiding principle for the optimum *failopt* choice, both options are evaluated in this effort.

3.3.2 Meshing

The mesh size dependency of capturing fracture within the context of shell model FEMs is a well-known drawback, and failure model and numerical method developers have expended much energy to alleviate it. Although it is possible to perform highly accurate analysis of the fracture process, a highly detailed 3D solid mesh is required to do so. Shell elements, in contrast, cannot possibly capture this level of detail. Furthermore, since the size of the fracture process zone (invariably smaller than the element size) is considered, it becomes clear that any fracture criteria must be tied to the element size. This can be achieved by adjusting the relevant fracture criteria, a process denoted “regularization,” to the length-to-thickness (l/t) ratio of the element. Although this a powerful and effective technique, a coordinated experimental and numerical analysis correlation effort is required to develop the failure-strain correction curves as a function

of *l*/*t*. Fortunately, past mesh size correction studies for modeling fracture of ductile steels, discussed by Nahshon and Miraglia (2011), provide conservative guidelines for optimal thin-shell element size according to *l*/*t*. A further requirement is that the mesh be sufficiently resolved to capture the stress state in the region of fracture, *l*/*t* ratios of over 8 or so being found to produce unrealistic answers for many loading cases. Conversely, *l*/*t* ratios close to unity amplify the mesh sensitivity of the fracture criteria due to the ability to crudely capture local necking phenomena and accompanying post-necking strains. Thus, it is advantageous to avoid overly refined meshes where post-necking strain can be ignored. For areas with *l*/*t* ratios below unity, a strain-field regularization scheme is required.

One major goal of the punched panel simulations was to demonstrate the adequacy of peak load and failure pattern predictions when using thin shell element meshes in the *l*/*t* range between 1 and 8. The stiffened NTNU specimens consisted of 6 mm thick flat bars welded to 5 mm thick flat plate. The FE meshes developed by the NTNU investigators utilized elements with 5, 10, and 18 mm lateral dimensions, giving *l*/*t* ratios for the 5 mm plating of 1.0, 2.0, and 3.6. It is of particular interest in this effort to establish the acceptability of meshes with *l*/*t* > 3.6. Accordingly, two bounding meshes with *l*/*t* ratios of 3.0 and 6.0 in the specimen flat plating were developed. An exactly intermediate mesh with *l*/*t* of 4.5 was not possible, so a mesh with *l*/*t* of 4 in the shorter lateral dimension and *l*/*t* of 4.286 in the longer lateral dimension was defined. For these three meshes, 6, 5, and 4 elements were specified through the flat bar depth dimension. The flat plate and support box meshes for the specimens with one and two flat bars were the same as for the unstiffened specimen, but the meshing accommodated flat bar positions for both the one- and two-bar specimens.

The nine FEMs for the three specimen types with three mesh densities are pictured in Figure 5, Figure 6, and Figure 7. These were developed with FE model generation tools available in the FEMAP engineering software package (FEMAP, 2019). NTNU had assumed that during testing, the rigid indenter would not be perfectly centered on the apparent geometric center of the nominally doubly symmetric panels. As a result, NTNU positioned the discretized indenter slightly off-center in their FEMs. Their stated assumption is indenter positioning “5 mm off the panel center” but they did not elaborate on whether the standoff was radial or aligned with the panel’s shorter and/or longer dimensions. Accordingly, the present simulations presumed a 5 mm offset with respect to both lateral panel dimensions or, equivalently, a radial offset of $5\sqrt{2}$ mm. Consequently, the nominal double symmetry of the panels could not be exploited in FEM definition.

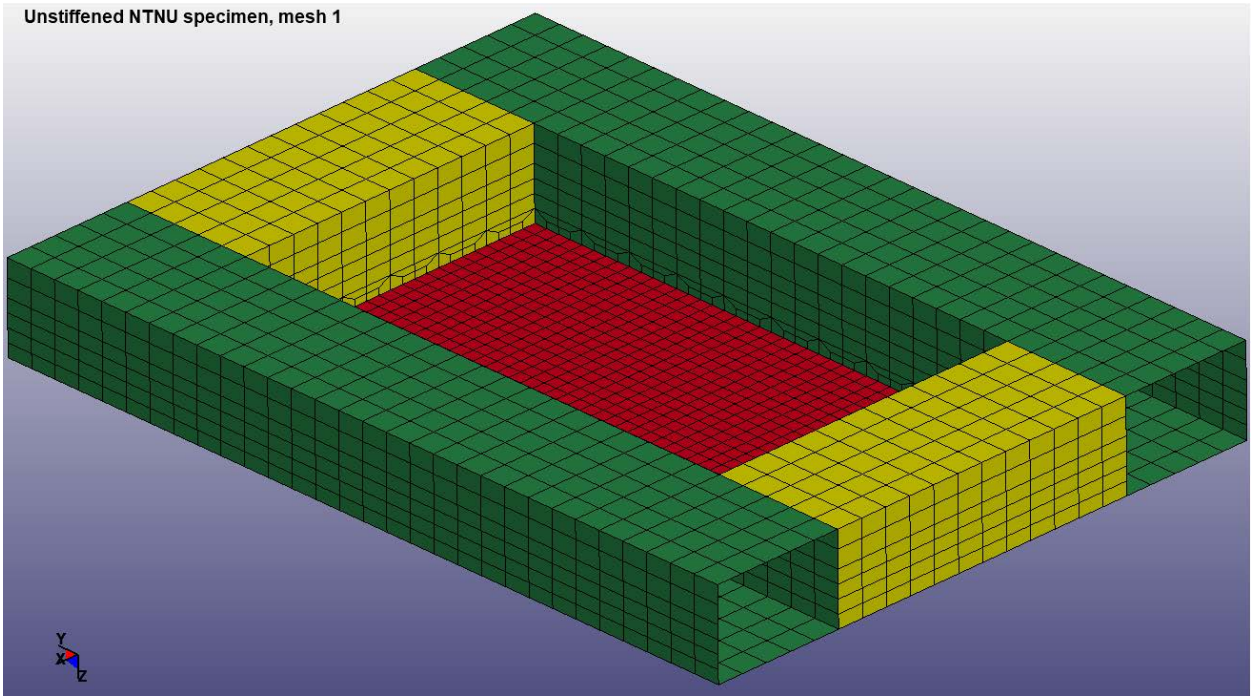

(a) *l/t* = 6.0

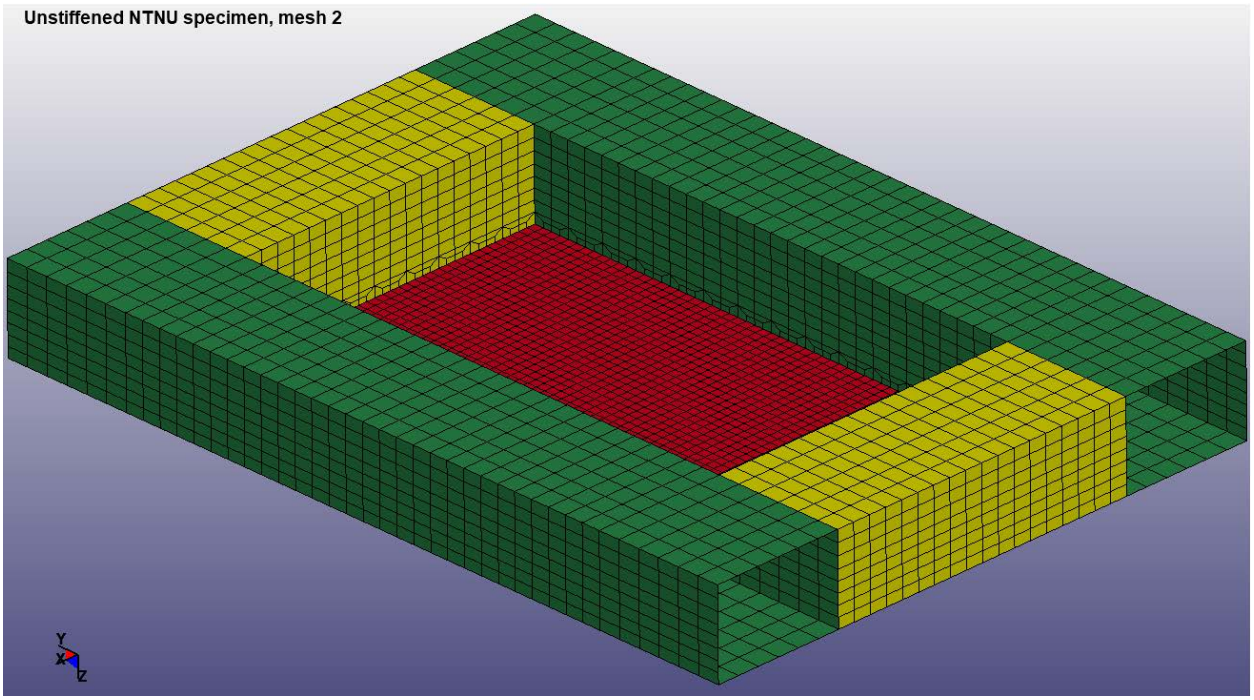

(b) *l/t* = 4.5

Figure 5. LS-DYNA Meshes for Unstiffened NTNU Specimen

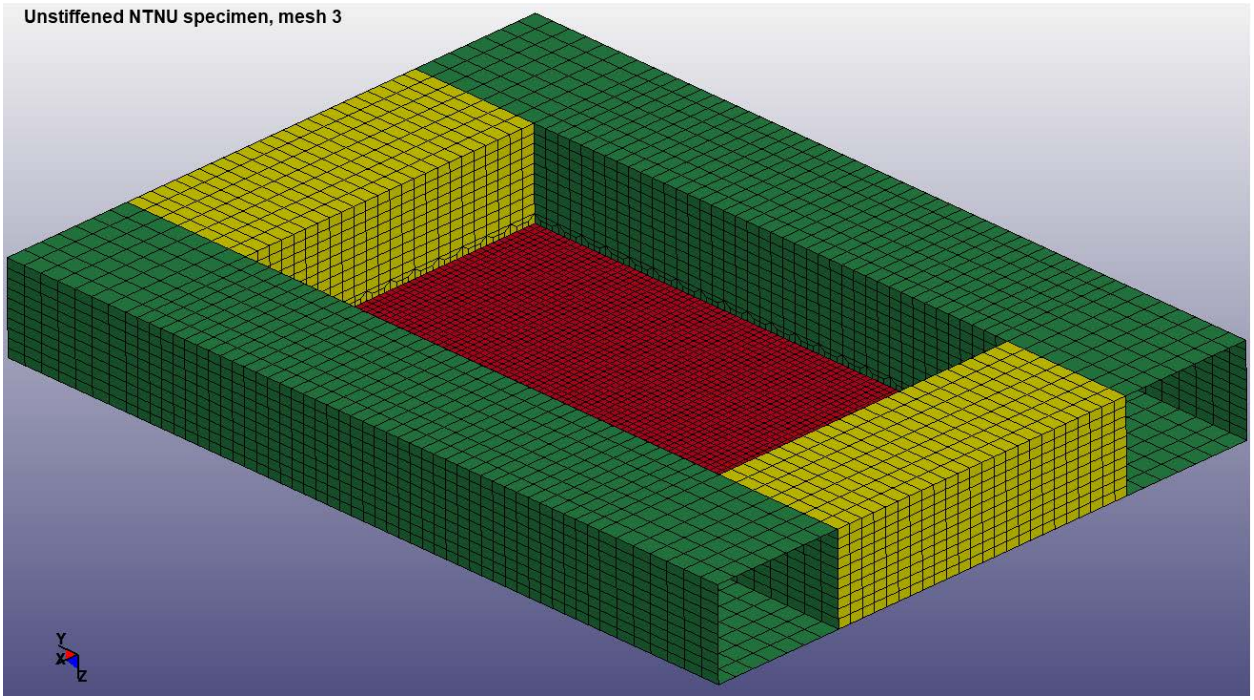

(c) *l*/*t* = 3.0

Figure 5. LS-DYNA Meshes for Unstiffened NTNU Specimen (cont'd)

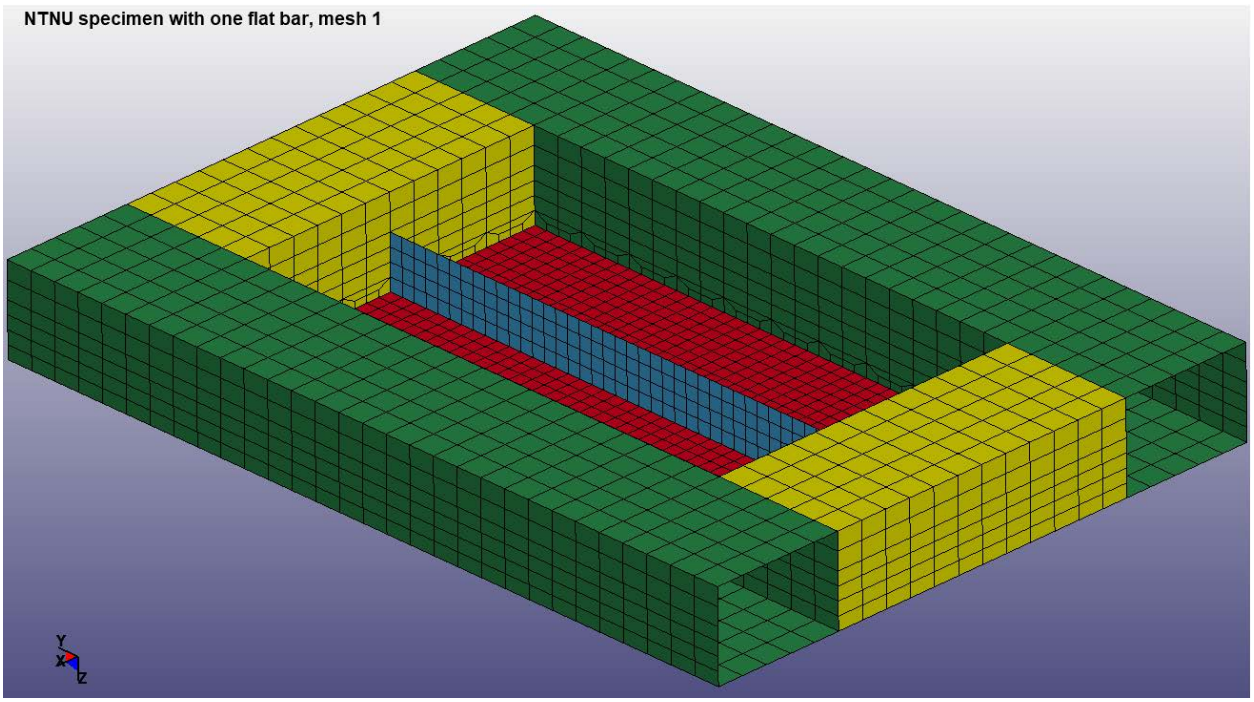

(a) *l*/*t* = 6.0

Figure 6. LS-DYNA Meshes for NTNU Specimen with One Flat Bar Stiffener

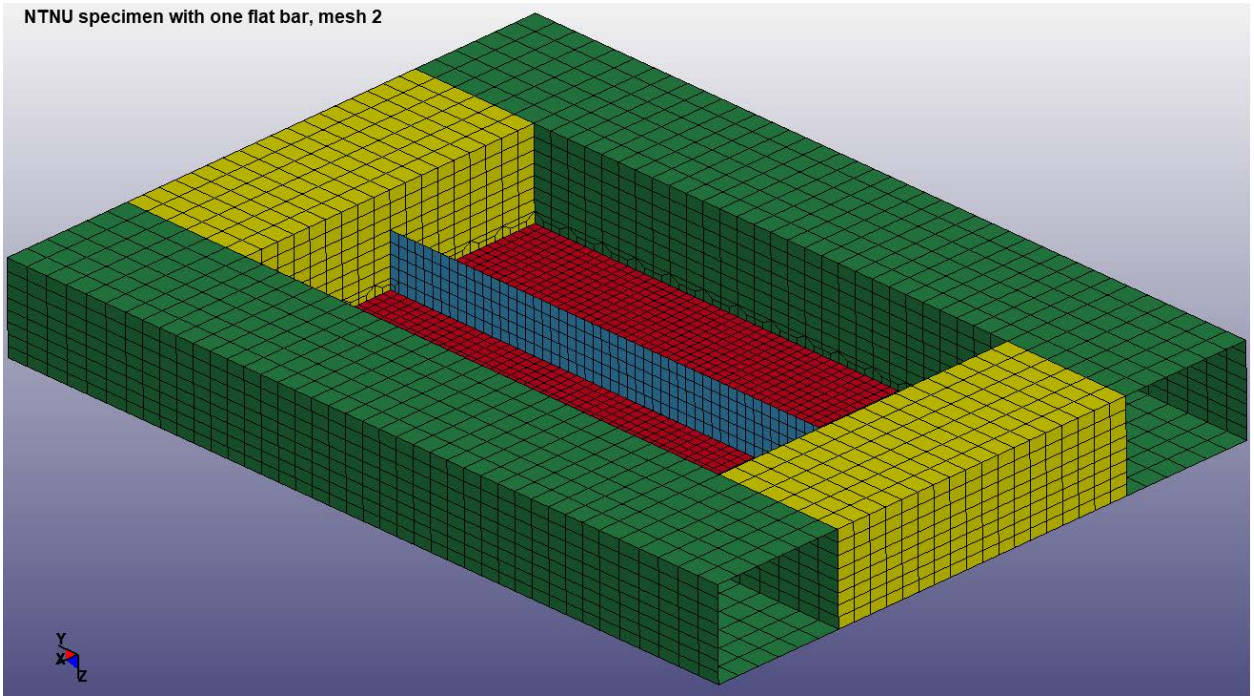

(b) *l*/*t* = 4.5

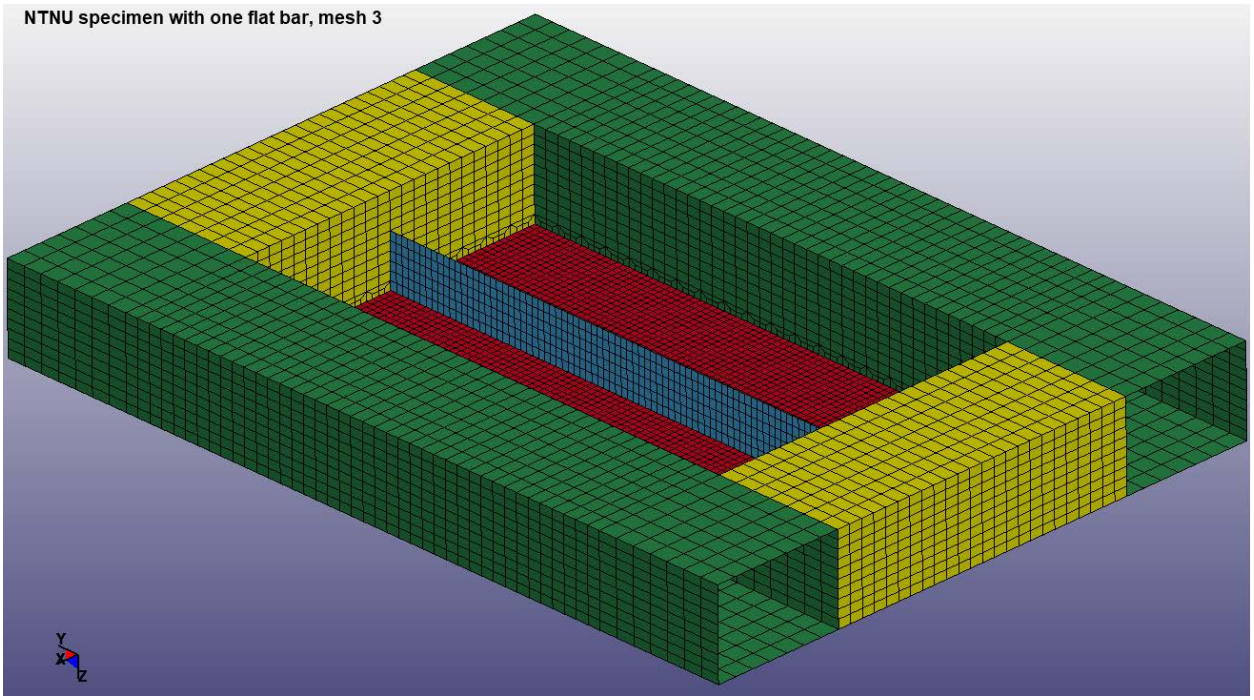

(c) *l*/*t* = 3.0

Figure 6. LS-DYNA Meshes for NTNU Specimen with One Flat Bar Stiffener (cont'd)

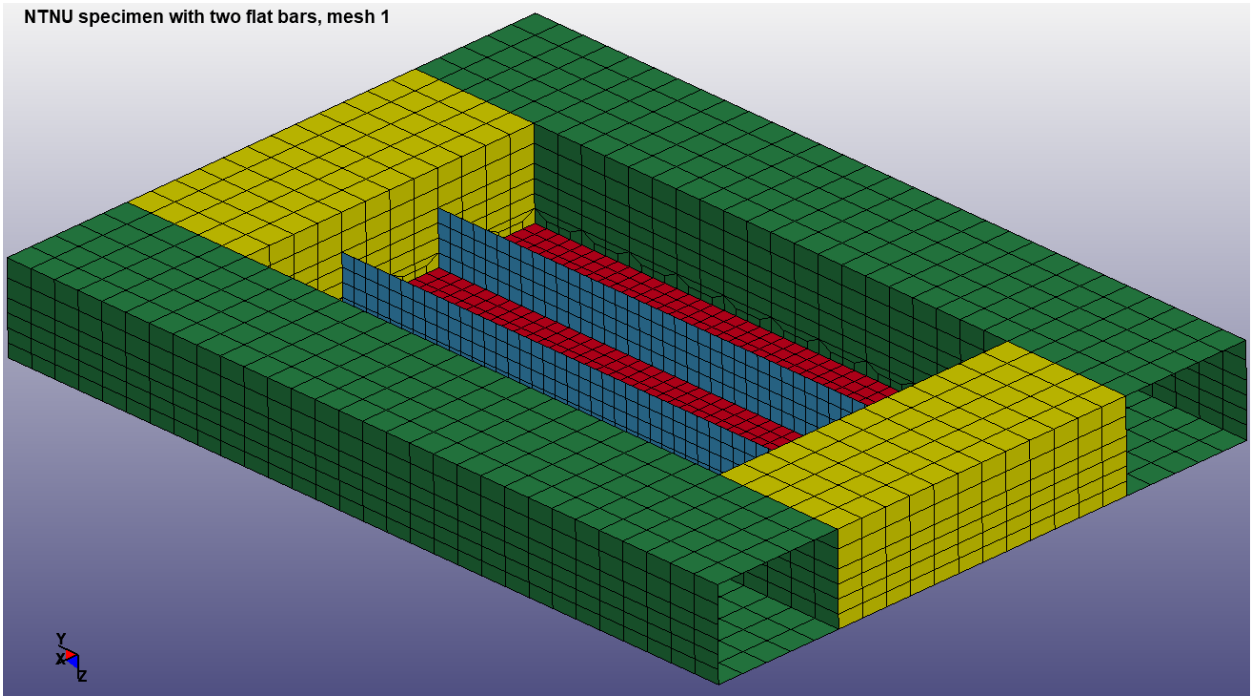

(a) *l/t* = 6.0

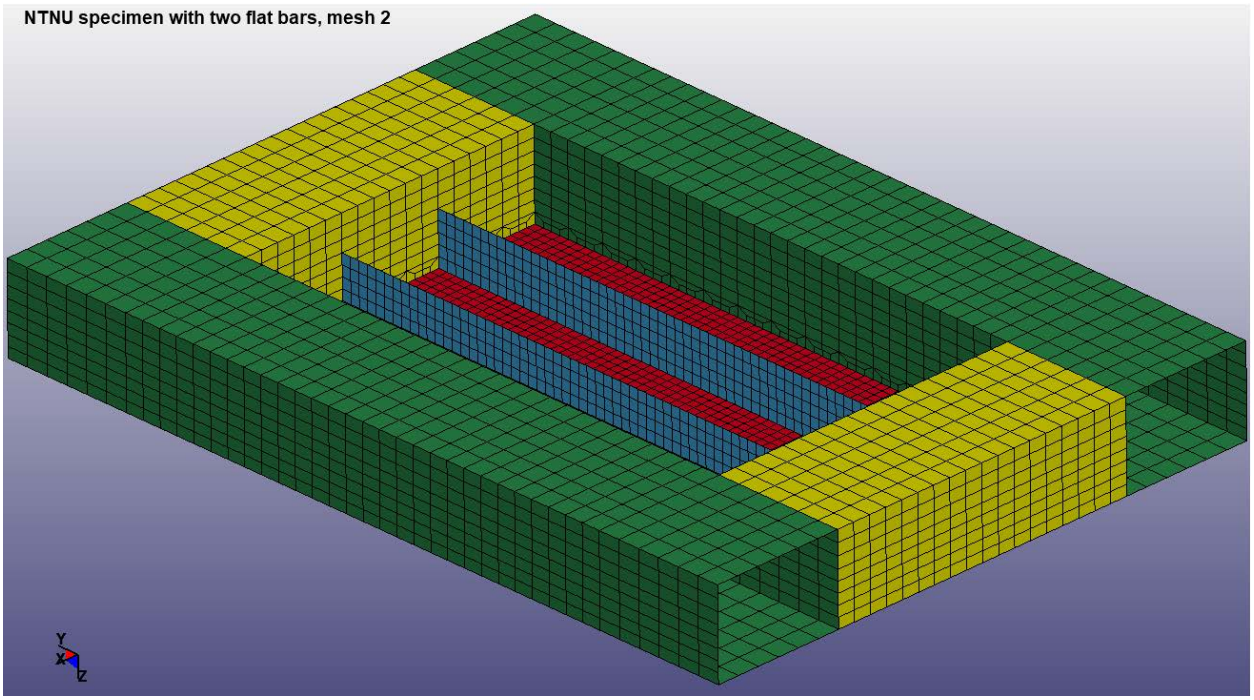

(b) *l/t* = 4.5

Figure 7. LS-DYNA Meshes for NTNU Specimen with Two Flat Bar Stiffeners

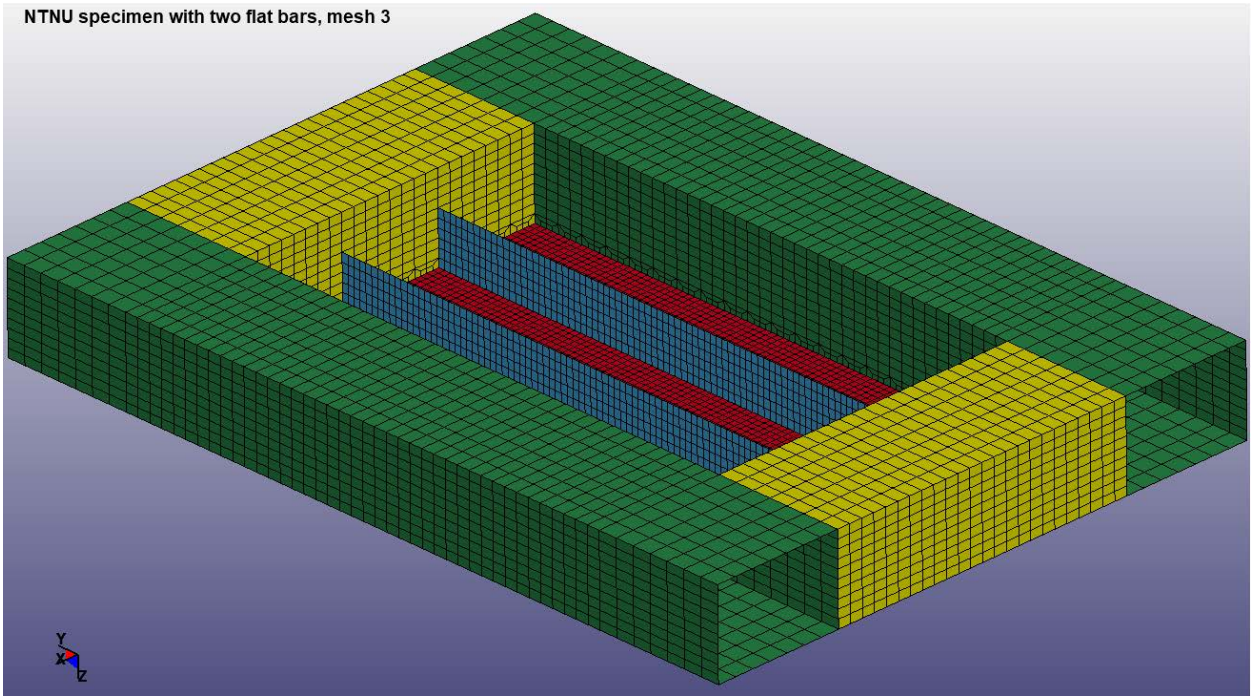

(c) *l*/*t* = 3.0

Figure 7. LS-DYNA Meshes for NTNU Specimen with Two Flat Bar Stiffeners (cont'd)

In addition, NTNU imposed initial imperfections "in the form of a sine curve" to all stiffeners, with an amplitude of 0.1 percent of stiffener length. A user-defined FEMAP script[3] carried out the required perturbations of the flat bar meshes, resulting in flat bar node lateral distortions in the form of a half-sine wave along bar lengths and a quarter-sine wave along bar depths. Maximum distortion occurs at bar midlengths and zero distortions prevail at the bar ends attached to the support boxes and bar bases adjoining the specimen flat plating (see Figure 8, which exaggerates these initial distortions). NTNU did not state whether the distortions of the two flat bars in the two-stiffener specimens were in-phase or out-of-phase, so an in-phase condition was randomly chosen. They also did not state whether the distortions reflected pinned or clamped end conditions at stiffener ends or bases, so pinned conditions were assumed in the present LS-DYNA models.

[3] FEMAP script was provided by Mr. Nathan Klontz, NSWCCD Code 652.

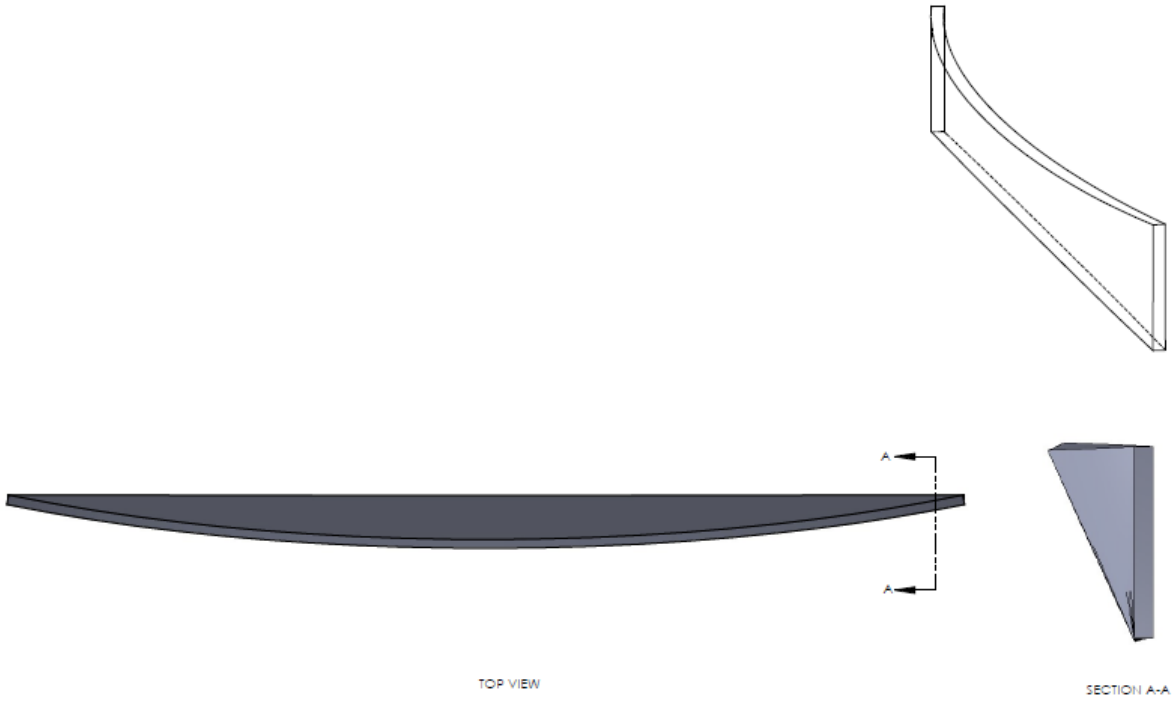

Figure 8. Initial Distortion Pattern Assumed in NTNU Specimen Flat Bars

Table 8 lists the number of nodes in the nine NTNU test article FEMs, not including the discretized indenter. Even for the densest mesh, the models are quite modest. The numbers 1, 2, and 3 refer to the coarse, medium, and fine meshes, respectively.

Table 8. LS-DYNA FEM Sizes for Three NTNU Test Article Meshes

Test Article Model Property	Test Article Type		
	Unstiffened (US)	One Flat Bar-Stiffened (1-FB)	Two Flat Bar-Stiffened (2-FB)
Mass (kg)	528.46	535.24	542.03
Mesh 1 *(l/t = 6.0)*	3001 nodes	3157 nodes	3313 nodes
Mesh 2 *(l/t = 4.5)*	5541 nodes	5820 nodes	6091 nodes
Mesh 3 *(l/t = 3.0)*	9529 nodes	10003 nodes	10477 nodes

3.3.3 Boundary Conditions, Loading, and Kinematics

Test specimen and support frame displacement and rotation boundary conditions follow NTNU assumptions and are the same for all five panels analyzed. All nodes on bottom surfaces of the stiff and massive support boxes are fully constrained against displacement and rotation in all six degrees of freedom. Figure 9 shows an example for a model with the densest mesh. The mesh is turned off in this figure for better visibility of the constrained nodes.

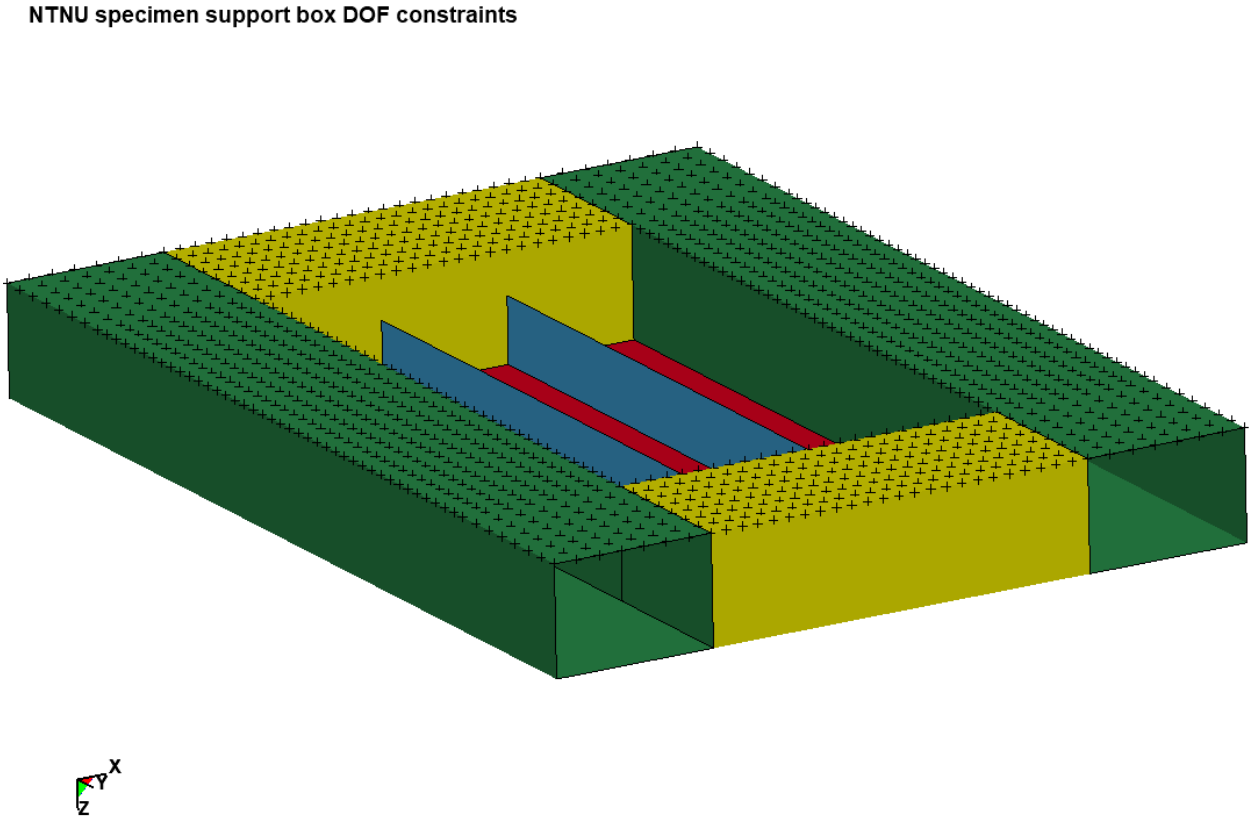

Figure 9. Boundary Conditions Imposed on NTNU Test Specimen Support Frames

The conical indenter with a spherically-contoured head is modeled with three-dimensional solid elements, LS-DYNA type -1 (8-point integration rather than default 1-point), and are assigned a perfectly rigid material. Given the rigid material and the virtually static rate of indenter movement, the whole volume of the indenter does not need to be meshed. The lateral dimensions of the indenter element's surfaces near the spherical head of the body are in the 14 to 15 mm range, and the depth of the 3D solids is a constant 10 mm. The same indenter idealization applied to all simulations, regardless of the test specimen mesh. Figure 10 illustrates the discretized rigid indenter.

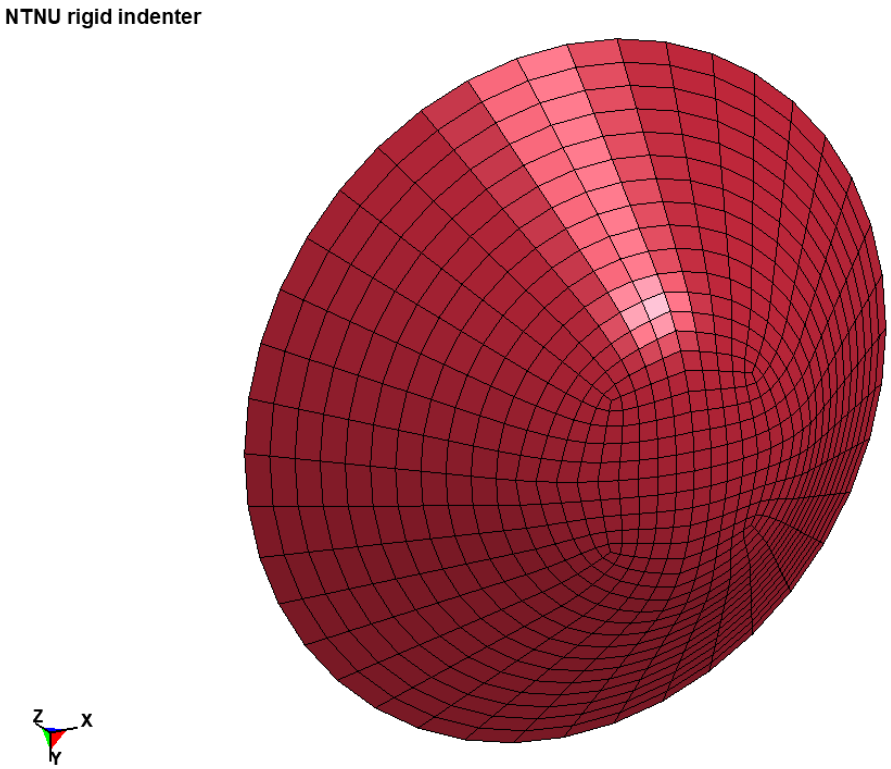

Figure 10. NTNU Rigid Indenter Modeling

All nodes on the rigid indenter are translated at a uniform time rate of displacement. Although the experimental loading rate of 10 mm/min in the NTNU punched panel tests is quite slow, NTNU assessed the need to account for strain-rate effects on steel strength in their test simulations. NTNU concluded that the effect on loads should be minor, on the order of 2 to 4 percent. As a consequence, strain rate effects were not accounted for in the present LS-DYNA simulations. However, the slow experimental loading rate poses an explicit-method time integration challenge. Experimental data for all specimens shows a need for analysis time durations such that as much as a 250 mm range of displacement is traversed. This implies that the LS-DYNA explicit analyses would need to cover 25 minutes of real time, a high burden given that critical time steps will be on the order of microseconds or smaller. Since strain rate effects are judged to be minor, the indenter displacement rate is scaled to be 1000 times faster than actual (1 m/6 s instead of 1 m/6000 s). Although this modeling artifice risks excitation of fundamental vibration modes of the specimens, the LS-DYNA simulations gave no sign of such excitation.

3.3.4 Other Assumptions

Contact between the test article plating and the rigid indenter is detected and tracked with the LS-DYNA single surface algorithm invoked by the CONTACT_AUTOMATIC_SINGLE_ SURFACE keyword. Surfaces allowed to participate in contact development are confined to the shell element-modeled flat plate and the lower surface of the 3D rigid indenter. Specimen stiffeners are confined to the underside of the plating and cannot become involved in indenter contact until well after flat plate rupture, if at all. Figure 11 illustrates contact surfaces designated for one selected LS-DYNA FEM. The mesh is turned off in this figure for better visibility of the element faces involved in the contact surface pair.

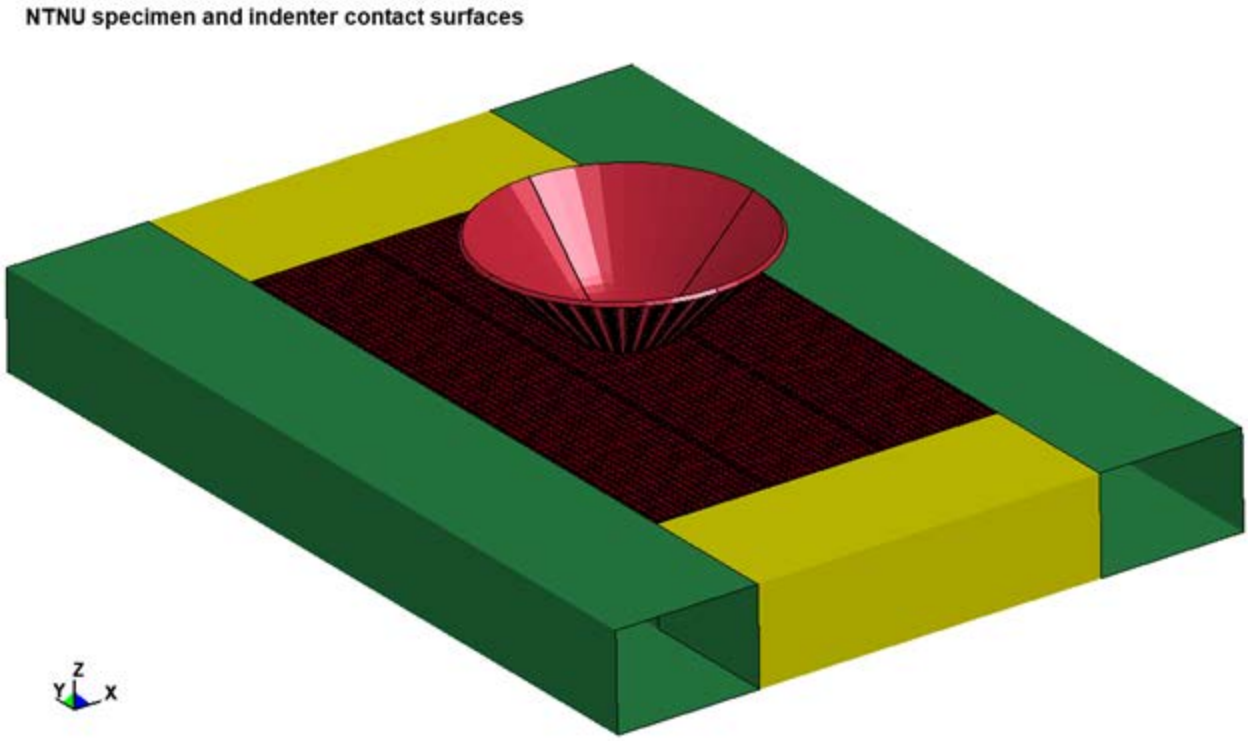

Figure 11. NTNU Test Specimen and Rigid Indenter Contact Surface Example

Figure 12 is a FEM cutaway view showing an example of indenter and test specimen positions at time zero. The z-direction offset between the lower surface of the indenter and the midplane of the specimen plate is 10 mm. Given the 5 mm plate thickness, the actual time-zero gap sensed by LS-DYNA is 7.5 mm. As mentioned above, the x,y position of the indenter apex is purposely offset slightly from the plate center point, 5 mm in both lateral dimensions.

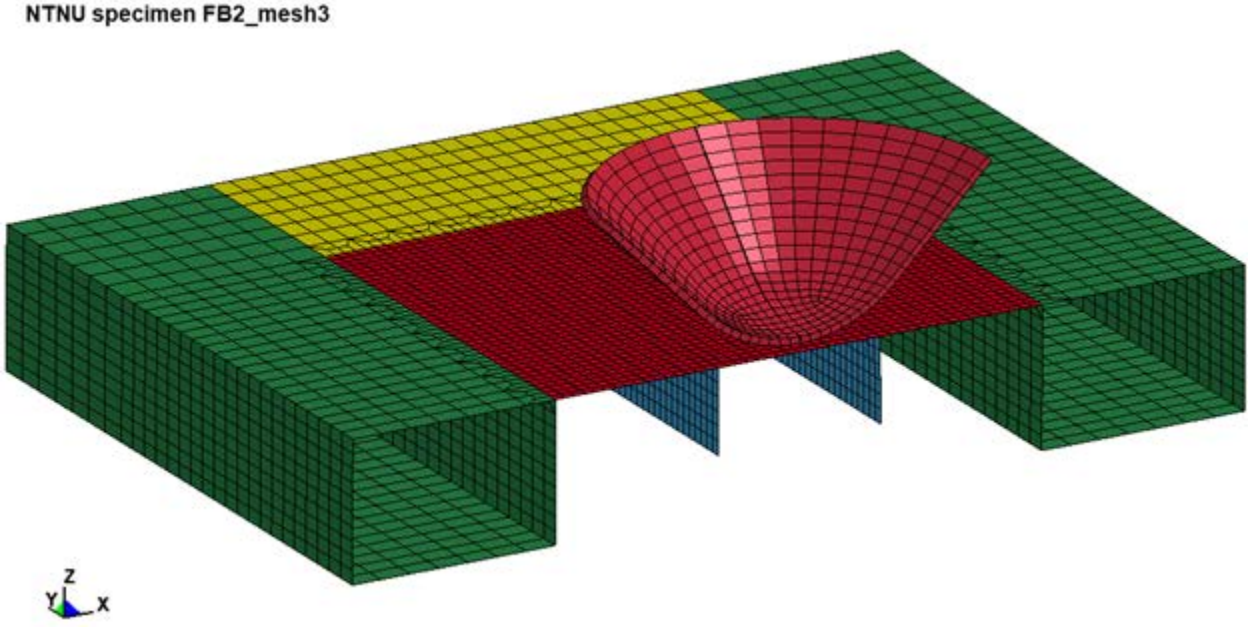

Figure 12. Rigid Indenter and NTNU Test Specimen Positions at Time Zero

LS-DYNA allows modeling of contact surface friction with classical Coulomb friction assumptions, and it allows optional assignment of distinct static and dynamic friction properties. NTNU assumed a static friction coefficient of 0.30, deemed as a reasonable assumption for friction at very slow relative sliding speed between coated steel surfaces. The same assumption applied to the present models. NTNU did not state usage of a nonzero dynamic friction coefficient, so moderately slow decay of static to dynamic friction as a function of velocity was assumed, with a decay constant (DC) of -1.0 and a dynamic friction coefficient of zero.

The LS-DYNA contact entity CONTACT_FORCE_TRANSDUCER_PENALTY recovers forces on all structural contact surface faces, the sum of which obtains the total load exerted on the test articles during loading progression. Time histories of this force are fundamental bases of comparison between the simulations for different meshes and with respect to the NTNU tests and analyses.

Following previous experience with its superior effectiveness in many analyses compared to the default viscous control method (Lesar, 2019, 2020), the stiffness hourglass control algorithm (option 4) was used with a coefficient of 0.10.

For modeler information, LS-DYNA computes the maximum time step implied by all structural elements and contact surfaces for explicit time integration stability. For all FEMs, the maximum time step implied by shell elements always governed over the contact surface time step. CONTROL_TIMESTEP-enforced time steps of 1.8, 1.5, and 1.2e-6 s were found appropriate to meshes 1, 2, and 3, respectively.

3.4 Simulation Hardware and Code Versions

U.S. Department of Defense High Performance Computing Center resources supported all simulations reported here, specifically, LS-DYNA code version 10 (mpp-s R10.1.0 rev 118243) installed on the Army Research Laboratory (ARL) computing systems. Computing hardware was the ARL SGI IceXA 2.6 PFLOPS 960-core platform *centennial*. Analyses of the NTNU specimens on *centennial* with LS-DYNA version 10 required 5.0 to 11.5 minutes of wall clock time for the coarsest and finest mesh models, respectively, with 80 processors requested in the “debug” job queue.

4. Results and Discussion

This major section describes the results of LS-DYNA simulations of the quasi-static and test specimens described in section 3.2. As described in section 3.3, each of three NTNU punch test articles were modeled with three systematically varing meshes. Analyses also considered usage of the binary 0 or 1 choice of the LS-DYNA ductile metal material model MAT224 parameter *failopt* governing the load-path (and time) dependency of effective plastic failure strain attainment. *Failopt* = 0 (default) triggers load-path dependence, wherein failure occurs when the time integral of effective plastic strain increments reaches the specified failure strain according to the current stress state. *Failopt* = 1 invokes load-path independence, wherein failure occurs when the current state of effective plastic strain reaches the specified stress state-dependent failure strain.

Table 9 through Table 11 lists particulars of the eighteen LS-DYNA runs accomplished for the three panel types, indicating meshes and failure parameter choices. Eighty *centennial* processors handled each case.

Table 9. Particulars of LS-DYNA Simulations of NTNU Unstiffened Panel Punch Tests

LS-DYNA Run ID	Mesh	Element *l/t*	Failure Option	Specified time step (s)	LS-DYNA Version	Wall-clock time
1579806	1 (coarse)	6.0	*failopt* 0	1.8e-6	10	5m 9s
1580002	2 (medium)	4.5	*failopt* 0	1.5e-6	10	6m 39s
1580171	3 (fine)	3.0	*failopt* 0	1.2e-6	10	9m 57s
1581818	1 (coarse)	6.0	*failopt* 1	1.8e-6	10	5m 9s
1581819	2 (medium)	4.5	*failopt* 1	1.5e-6	10	7m 51s
1581821	3 (fine)	3.0	*failopt* 1	1.2e-6	10	10m 27s

Table 10. Particulars of LS-DYNA Simulations of NTNU Panel Punch Tests on Panels with One Flat Bar Stiffener

LS-DYNA Run ID	Mesh	Element *l/t*	Failure Option	Specified time step (s)	LS-DYNA Version	Wall-clock time
1585260	1 (coarse)	6.0	*failopt* 0	1.8e-6	10	5m 21s
1585261	2 (medium)	4.5	*failopt* 0	1.5e-6	10	8m 29s
1585262	3 (fine)	3.0	*failopt* 0	1.2e-6	10	10m 24s
1586230	1 (coarse)	6.0	*failopt* 1	1.8e-6	10	5m 45s
1586236	2 (medium)	4.5	*failopt* 1	1.5e-6	10	8m 24s
1586237	3 (fine)	3.0	*failopt* 1	1.2e-6	10	10m 55s

Table 11. Particulars of LS-DYNA Simulations of NTNU Panel Punch Tests on Panels with Two Flat Bar Stiffeners

LS-DYNA Run ID	Mesh	Element *l/t*	MAT224 Failure Option	Specified time step (s)	LS-DYNA Version	Wall-clock time
1592004	1 (coarse)	6.0	*failopt* 0	1.8e-6	10	5m 26s
1592005	2 (medium)	4.5	*failopt* 0	1.5e-6	10	7m 22s
1592006	3 (fine)	3.0	*failopt* 0	1.2e-6	10	11m 11s
1592007	1 (coarse)	6.0	*failopt* 1	1.8e-6	10	5m 23s
1592009	2 (medium)	4.5	*failopt* 1	1.5e-6	10	7m 27s
1592010	3 (fine)	3.0	*failopt* 1	1.2e-6	10	11m 35s

The following three subsections provide LS-DYNA simulation results for the three test article types, with comparisons of computed failure loads and indenter displacements at failure to NTNU test data. Computed specimen tearing patterns are compared with experimental outcomes and LS-DYNA results are also compared with prior simulations (Alsos, Amdahl, and Hopperstad, 2009; AbuBakar and Dow, 2013).

4.1 Unstiffened Panel Specimens

Table 12 compares LS-DYNA-computed and experimental maximum indenter/specimen contact force resultants (peak loads at failure) and indenter displacements at failure for the six unstiffened specimen simulation cases listed in Table 9. The indenter displacement data omits the small indenter traversal distance prior to specimen plate contact.

Table 12. Comparison of LS-DYNA Computed Failure Conditions with NTNU Test Data for Unstiffened Panel

LS-DYNA Run ID	Mesh	MAT224 Failure Option	Maximum Contact Force (kN)	Indenter Displacement at Peak Force (mm)
1579806	1 (coarse)	*failopt* 0	1579.9	188.7
1580002	2 (medium)	*failopt* 0	1492.3	182.5
1580171	3 (fine)	*failopt* 0	1542.0	186.7
1581818	1 (coarse)	*failopt* 1	1513.7	183.5
1581819	2 (medium)	*failopt* 1	1410.4	176.0
1581821	3 (fine)	*failopt* 1	1421.8	177.2
Experimental Data			1488	202.5

Figure 13 compares LS-DYNA-computed indenter force versus displacement curves for the unstiffened panel specimen with NTNU-measured data. The jog in the experimental curve at 130 mm displacement resulted from loading apparatus reset at maximum stroke. The computed trends are quantitatively correct, though discernible scatter exists between results for the three meshes and the two failure condition definition options of MAT224.

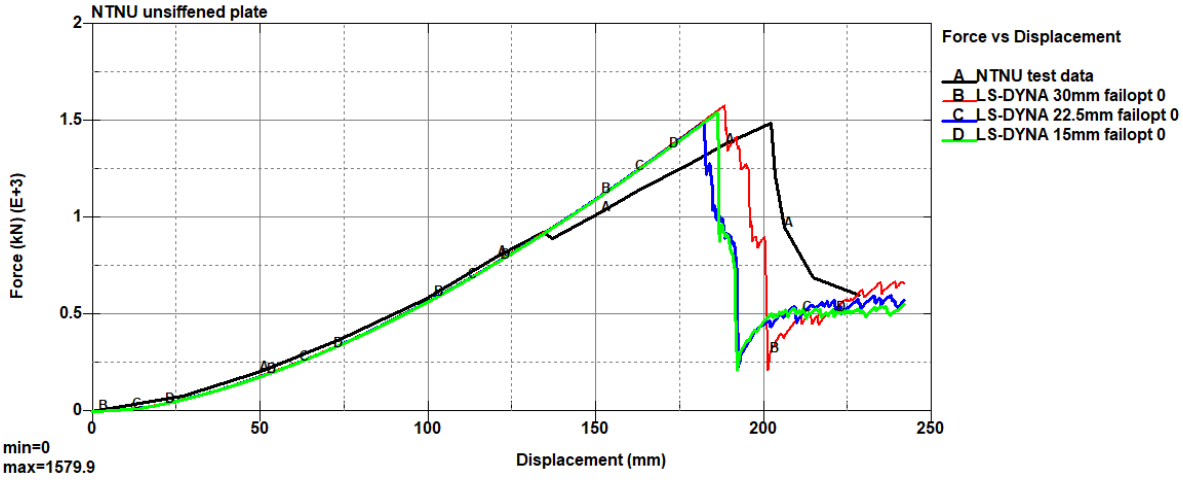

(a) *Failopt* = 0

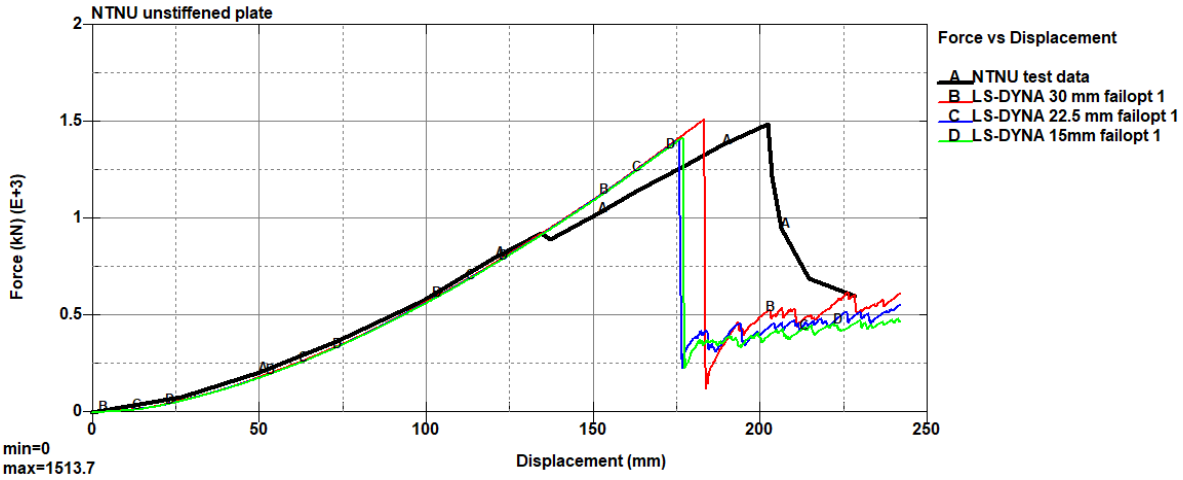

(b) *Failopt* = 1

Figure 13. Comparison of LS-DYNA-Computed Indenter Force versus Displacement Curves with NTNU Test Data for Unstiffened Panels

Figure 14 attempts to interpret the scatter evident in the results pictured in Figure 13. In this figure, peak load is plotted as a function of LS-DYNA shell element *l/t* ratio with separate curves for the two MAT224 failure condition definition options. Peak load as a function of *l/t* is also plotted for the LS-DYNA and ABAQUS analyses documented by Alsos, Amdahl, and Hopperstad (2009) and AbuBakar and Dow (2013), respectively. Note that the NTNU investigators employed generally denser meshes than this work and AbuBakar and Dow. The NTNU results pertain to the BWH failure criterion, which exhibited much less mesh sensitivity than the RTCL criterion (see discussion of these criteria in section 3.3.1).

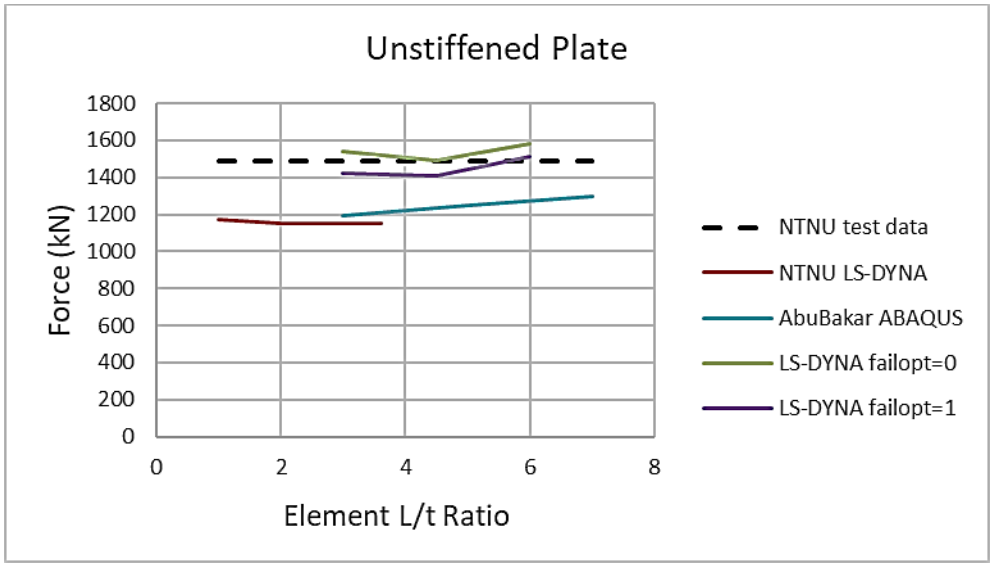

Figure 14. Unstiffened Panel Peak Load versus Element Size Ratio

Figure 14 indicates an improvement of LS-DYNA peak load predictions compared to the prior published simulations. For the medium and finer meshes, LS-DYNA peak loads for *failopt* = 0 and *failopt* = 1 bracket the experimental peak load from above and below, respectively. Since Alsos et al. and AbuBakar and Dow did not document every assumption of their analyses, it is impossible to attribute specific factors to their low peak load predictions.

The correctness of the LS-DYNA computed tearing patterns exhibited by the ruptured plate FEMs is now considered. The experimental rupture and tearing outcome was a single simple slightly-arced crack on one side of the indenter, roughly oriented parallel to the longer plate dimension. Figure 15 illustrates LS-DYNA-computed crack patterns from the first few full-model binary database data-writing steps after the start of element failure for the *failopt = 0* option. Initial single-sided tears rapidly develop into two-sided tears, which later become U-shaped. Crack paths are able to become more curvilinear as mesh fineness increases. Also, the time span of damage progression shortens as mesh is refined.

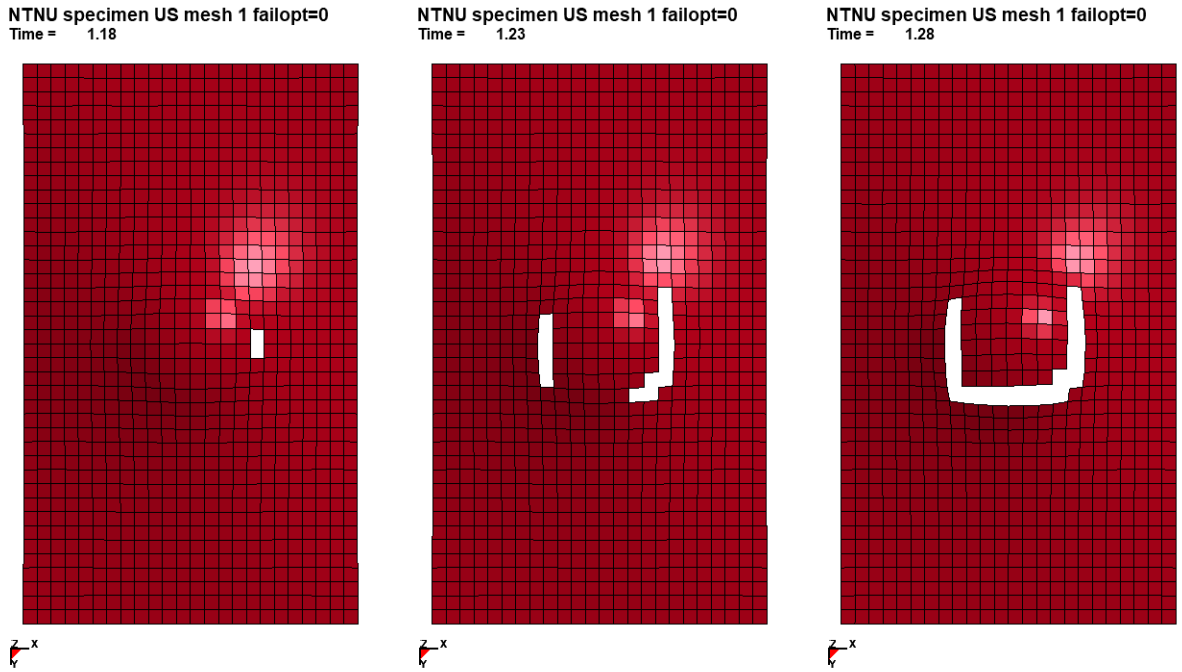

(a) *l/t* = 6

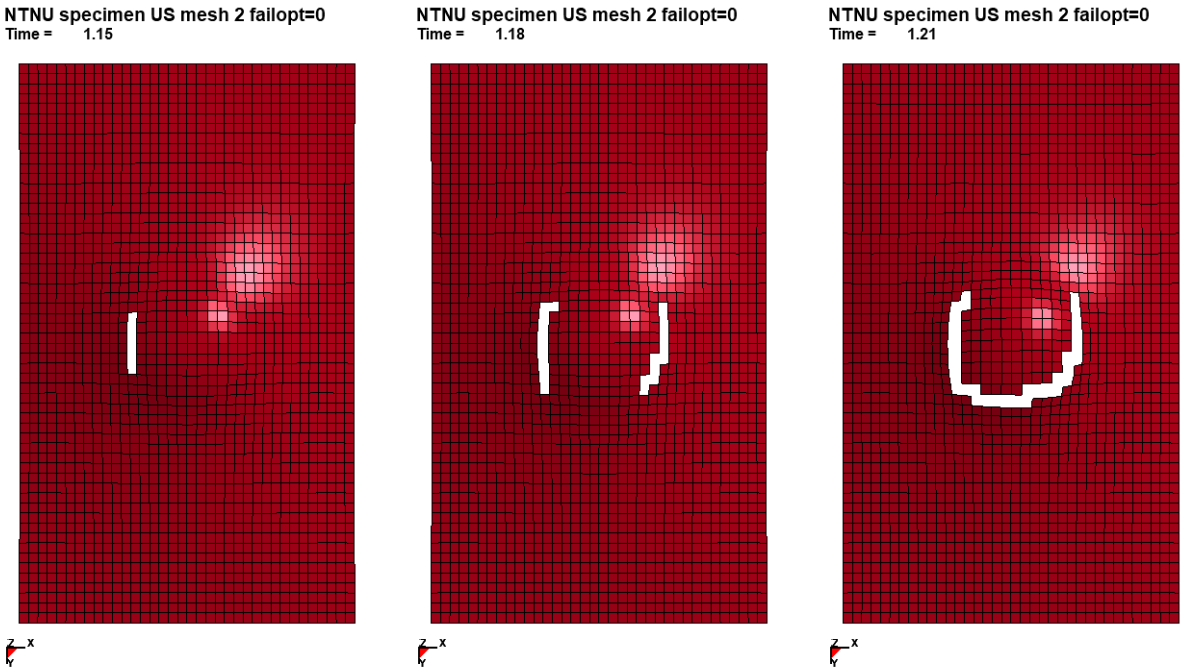

(b) *l/t* = 4.5

Figure 15. LS-DYNA-Computed Initial Tearing Patterns in Unstiffened Plate, *failopt* = 0

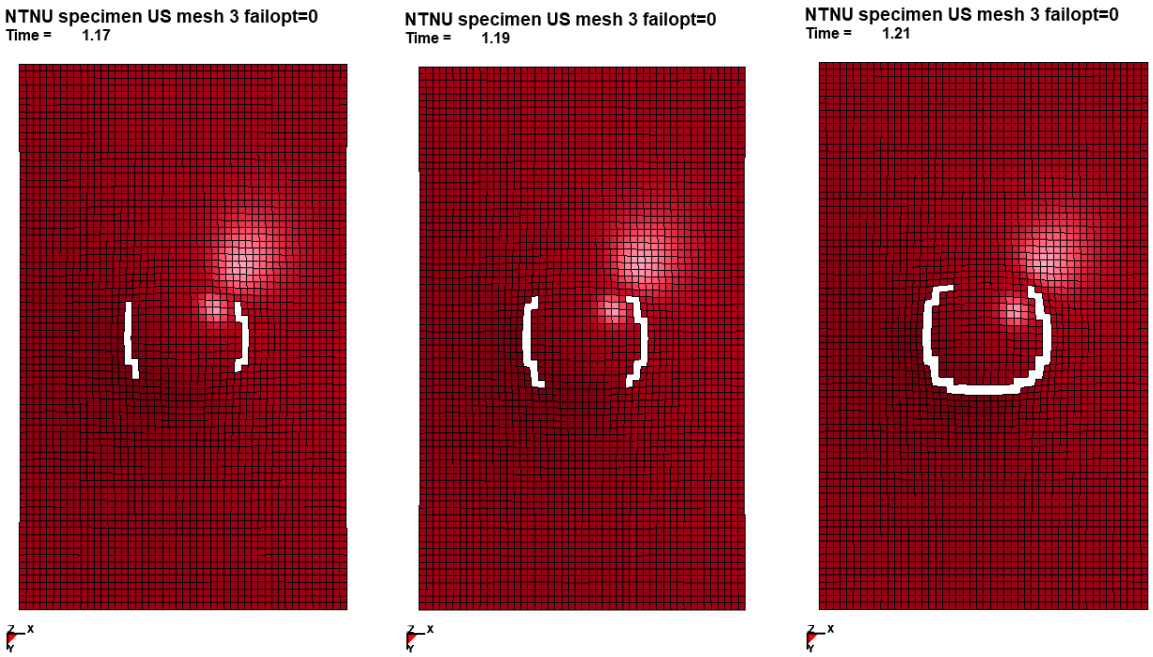

(c) *l/t* = 3

Figure 15. LS-DYNA-Computed Initial Tearing Patterns in Unstiffened Plate, *failopt* = 0 (cont'd)

Figure 16 provides similar data for the *failopt = 1* option. In contrast to *failopt = 0*, initial tears are curvilinear, even for the coarsest mesh. Several secondary cracks branched from the initial curved crack during later times.

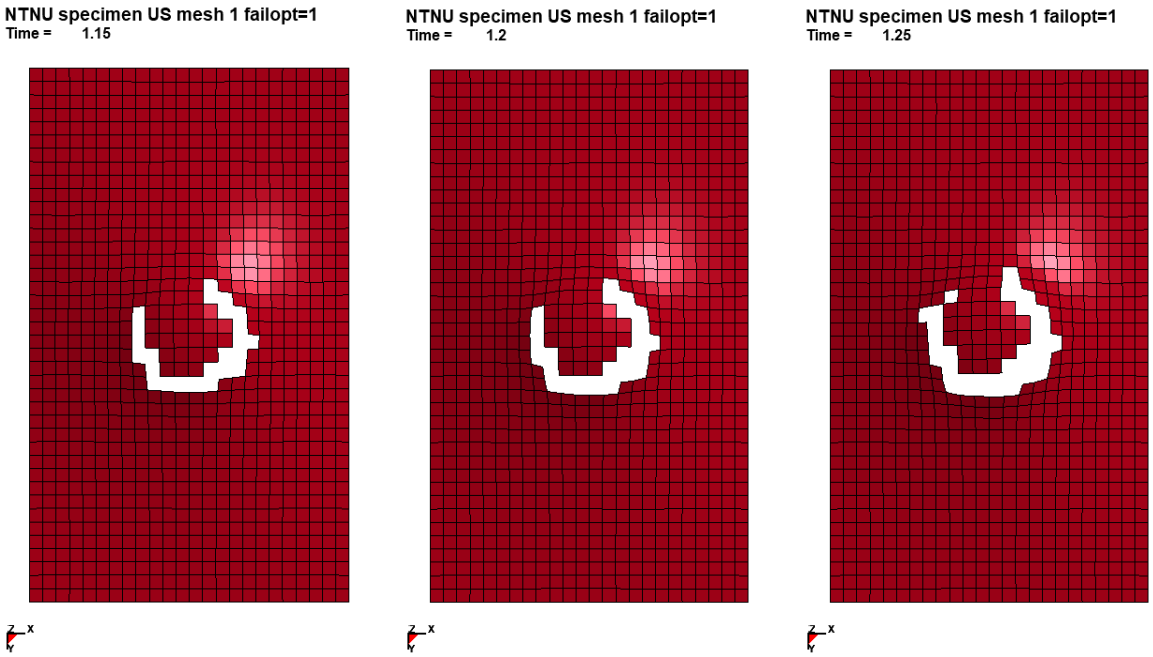

(a) *l/t* = 6

Figure 16. LS-DYNA-Computed Tearing Patterns in Unstiffened Plate, *failopt* = 1

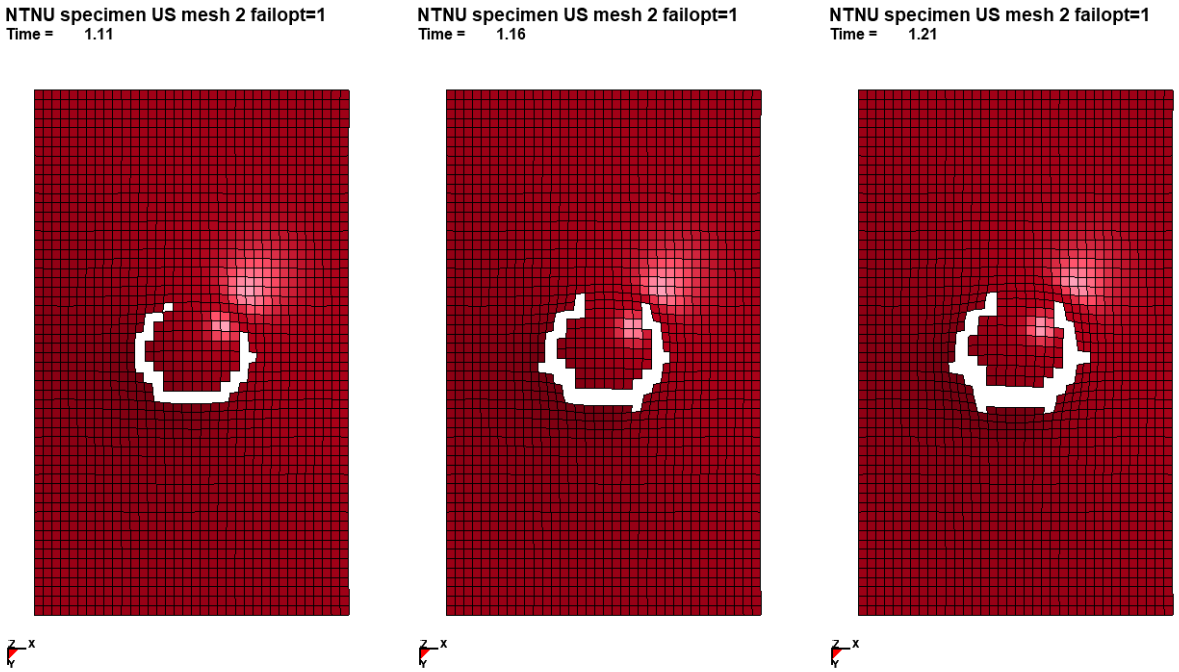

(b) *l/t* = 4.5

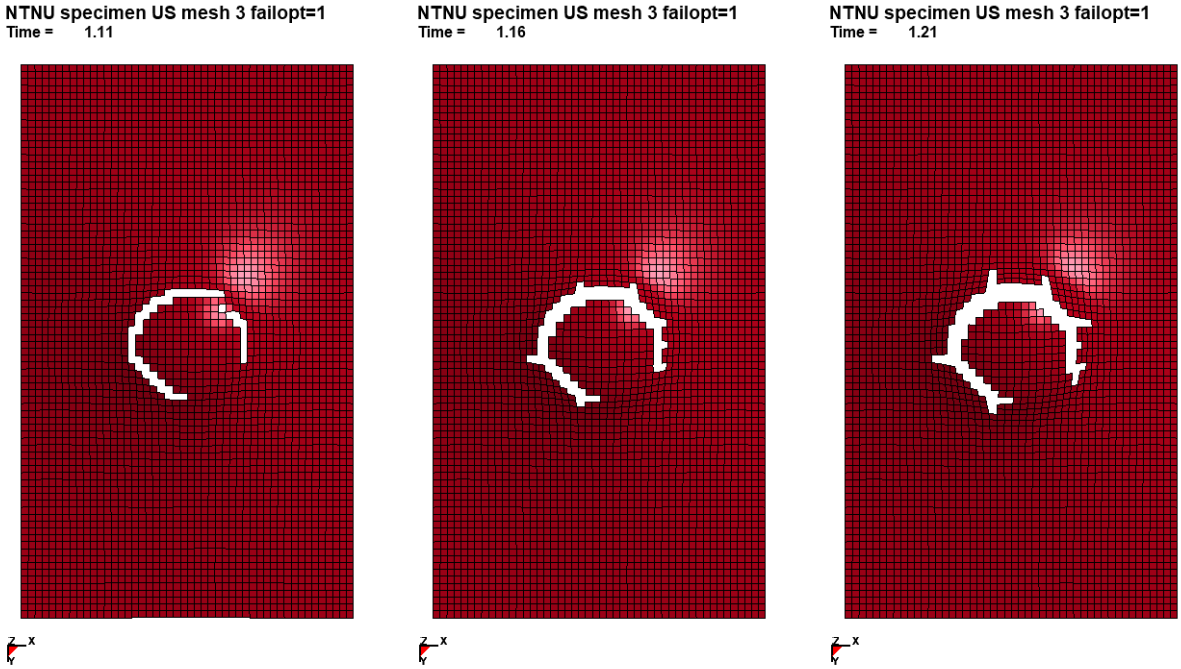

(c) *l/t* = 3

Figure 16. LS-DYNA-Computed Tearing Patterns in Unstiffened Plate, *failopt* = 1 (cont'd)

For the unstiffened plate, it is difficult to conclude any superiority of LS-DYNA failure load and tearing pattern computations for either of the plastic strain path-dependency options. The (default) path-dependent and the path-independent options bracketed the measured failure load from above and below, respectively, and both options yielded tearing pattern features resembling experimental results. It could be argued that the path-independent option yielded more conservative predictions indicating “weaker” fracture resistance.

4.2 Specimens Stiffened by One Flat Bar

Table 13 compares LS-DYNA-computed and experimental maximum indenter/specimen contact force resultants (peak loads at failure) and indenter displacements at failure for the six single flat bar-stiffened specimen simulation cases listed in Table 10. The indenter displacement data omits the small indenter traversal distance prior to specimen plate contact.

Table 13. Comparison of LS-DYNA Computed Failure Conditions with NTNU Test Data for Flat Bar-Stiffened Panel 1-FB

LS-DYNA Run ID	Mesh	MAT224 Failure Option	Maximum Contact Force (kN)	Indenter Displacement at Peak Force (mm)
1585260	1 (coarse)	*failopt* 0	1501.7	171.5
1585261	2 (medium)	*failopt* 0	1615.8	180.5
1585262	3 (fine)	*failopt* 0	1438.0	168.2
1586230	1 (coarse)	*failopt* 1	1384.2	162.0
1586236	2 (medium)	*failopt* 1	1506.4	172.3
1586237	3 (fine)	*failopt* 1	1297.0	156.5
Experimental Data			1417	172.0

Figure 17 compares LS-DYNA-computed indenter force versus displacement curves for the single flat bar-stiffened panel specimen with NTNU-measured data. The jog in the experimental curve at 130 mm displacement resulted from loading apparatus reset at maximum stroke. As with the unstiffened panel, the computed trends seem to be correct, though discernible scatter exists between results for the three meshes and the two failure condition definition options of MAT224.

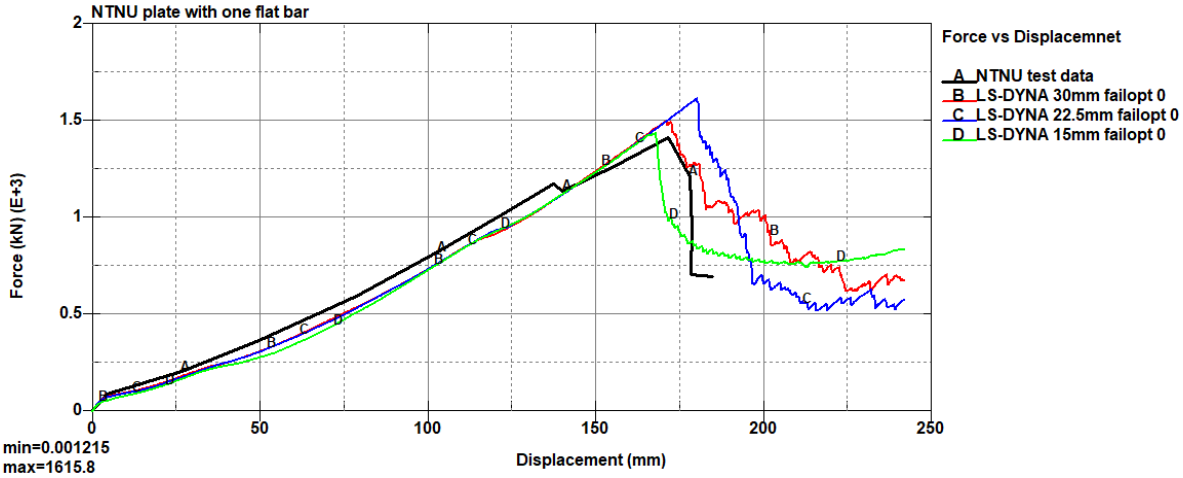

(a) *Failopt* = 0

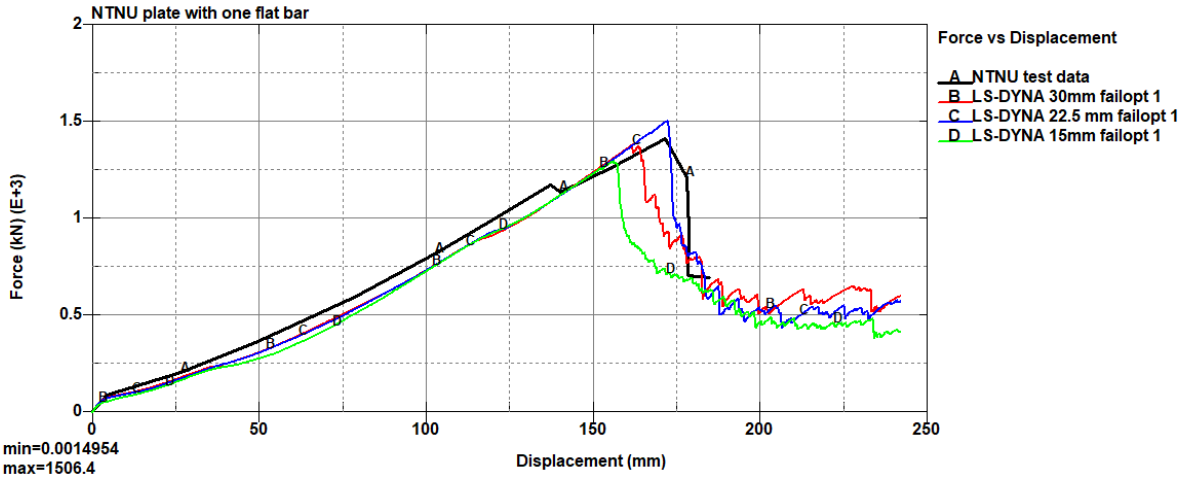

(b) *Failopt* = 1

Figure 17. Comparison of LS-DYNA-Computed Indenter Force versus Displacement Curves with NTNU Test Data for FB-1 Panels

Figure 18 attempts to interpret the scatter evident in the results pictured in Figure 17. In this figure, peak load is plotted as a function of LS-DYNA shell element *l/t* ratio with separate curves for the two MAT224 failure condition definition options. Peak load as a function of *l/t* is also plotted for the LS-DYNA and ABAQUS analyses documented by Alsos, Amdahl, and Hopperstad (2009) and AbuBakar and Dow (2013), respectively.

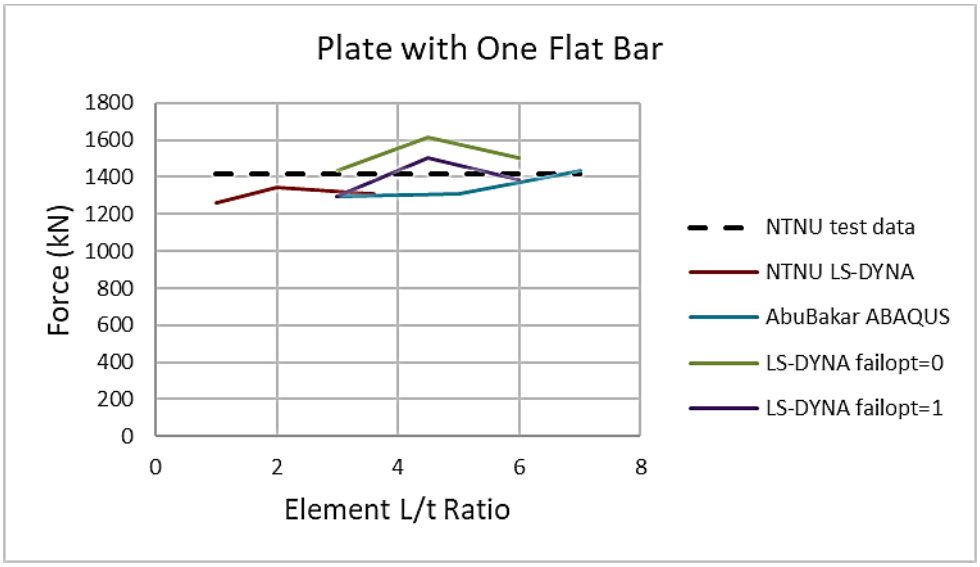

Figure 18. FB-1 Panel Peak Load versus Element Size Ratio

Figure 18 indicates more irregularity in LS-DYNA peak load predictions as a function of element size than for the unstiffened plate and for this stiffened plate examined by the other investigators. This behavior must be understood in the context of LS-DYNA-computed crack pattern correctness for the three meshes considered.

For the FB-1 specimen, the experimental outcome was a single linear tear close to one side of the plate/flat bar welded joint. Figure 19 illustrates LS-DYNA-computed crack patterns from the first few full-model binary database data-writing steps after the start of element failure for the *failopt = 0* option. For all three meshes, single linear tears initially develop, though the crack is (correctly) adjacent to the stiffener only in the finest mesh case. For the coarse and medium meshes, a second tear develops on the other side of the stiffener and a bridging crack develops across the stiffener itself, producing t- or h-shaped tears that did not occur in testing. Note also the extreme deformation of the flat bar, which bends so severely that it appears to “pass through” the supporting plate. If such deformation occurred, the flat bar would contact the plate. Such contact is not modeled in these simulations.

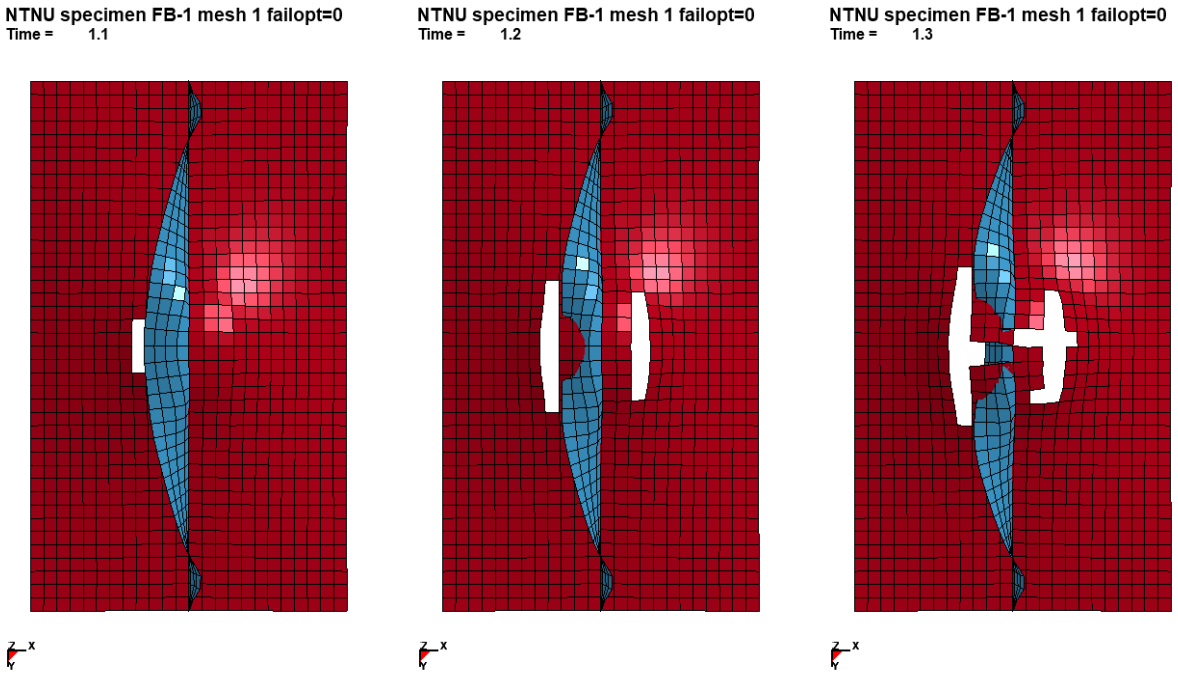

(a) *l/t* = 6

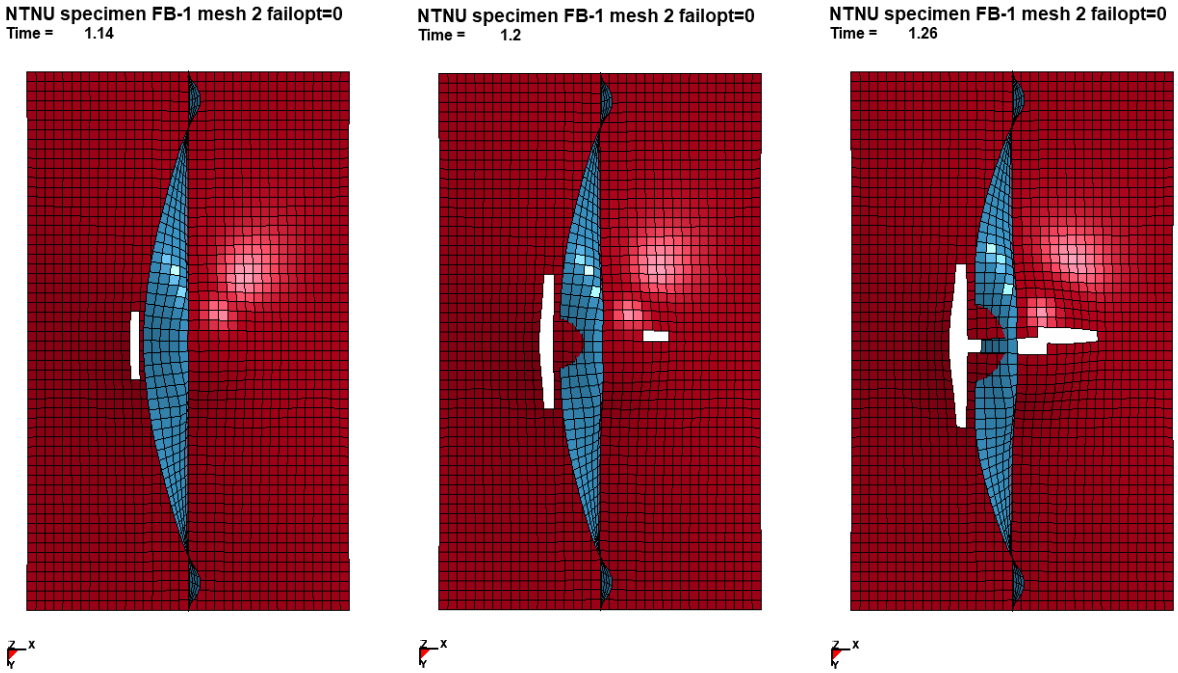

(b) *l/t* = 4.5

Figure 19. LS-DYNA-Computed Tearing Patterns in FB-1, *failopt* = 0

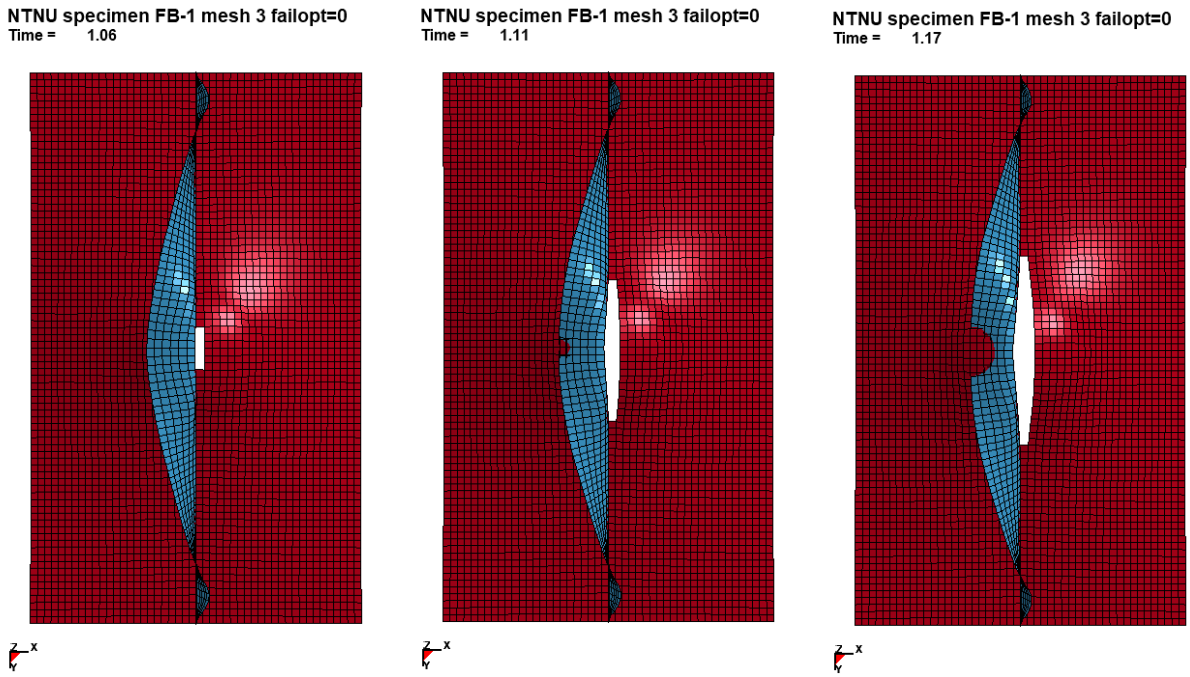

(c) *l/t* = 3

Figure 19. LS-DYNA-Computed Tearing Patterns in FB-1, *failopt* = 0 (cont'd)

Figure 20 provides similar data for the *failopt = 1* option. As in the previously discussed *failopt = 0* cases, only the finest mesh produces crack predictions resembling the experimental outcome, although the single crack following the stiffener joint sprouts secondary cracks across the stiffener at later times, which was not experimentally observed.

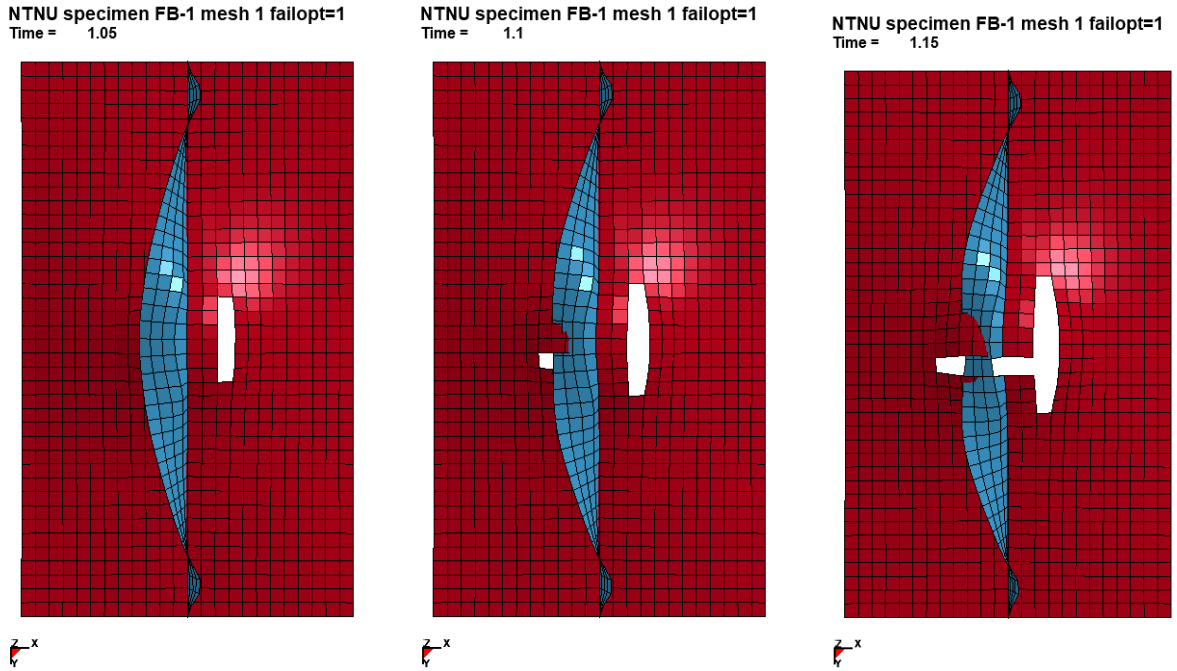

(a) *l/t* = 6

Figure 20. LS-DYNA-Computed Tearing Patterns in FB-1, *failopt* = 1

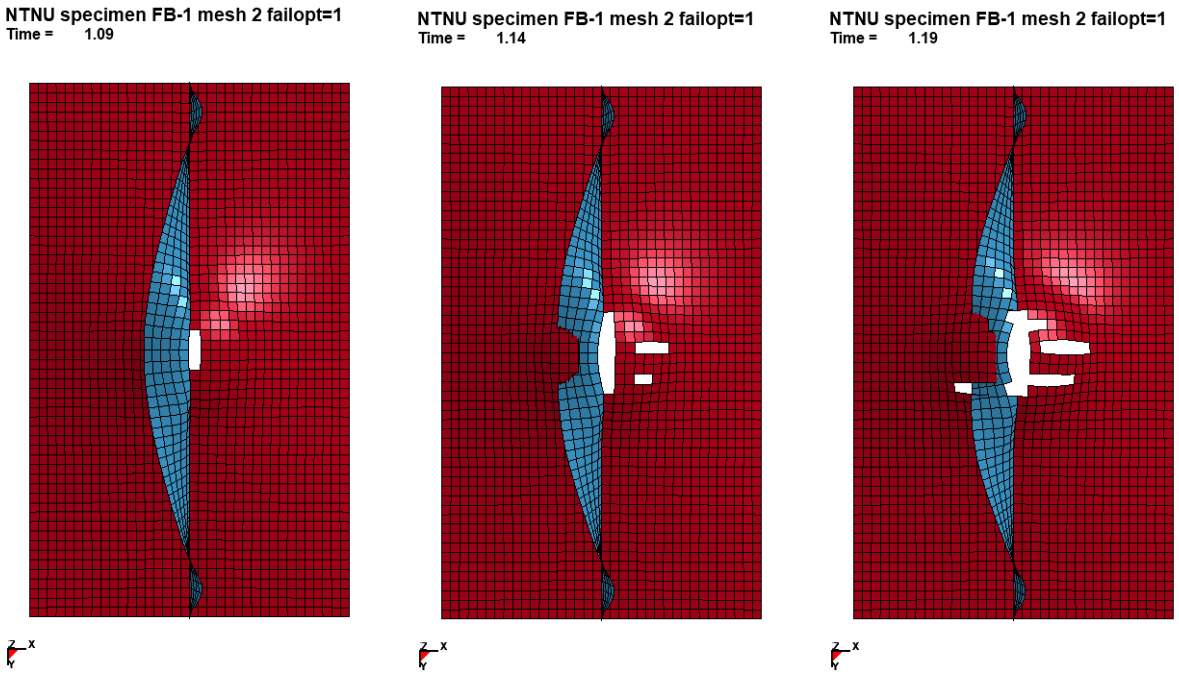

(b) *l/t* = 4.5

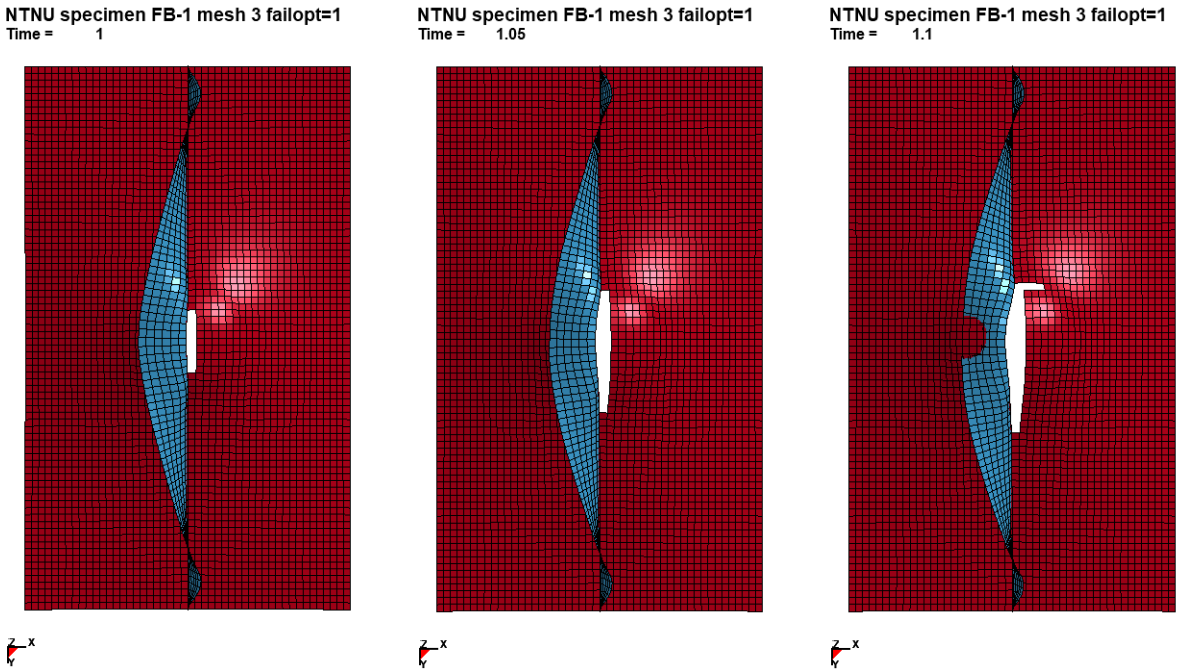

(c) *l/t* = 3

Figure 20. LS-DYNA-Computed Tearing Patterns in FB-1, *failopt* = 1 (cont'd)

For the plate stiffened by a single flat bar with the plating opposite the flat bar directly loaded, it is clear that mesh density dramatically affects the quality of failure process prediction, almost certainly because only the finest mesh resolves the high strain gradient present at the plate/stiffener joint. Since only the finest mesh produced reasonable failure pattern predictions,

only the fine mesh results can be used to draw conclusions regarding the two MAT224 path-dependence options. In the FB-1 case, the path-dependent *failopt = 0* provided good failure load and crack pattern accuracy while the path-independent *failopt = 1* option yielded a more conservative prediction indicating "weaker" fracture resistance.

4.3 Specimens Stiffened by Two Flat Bars

Table 14 compares LS-DYNA-computed and experimental maximum indenter/specimen contact force resultants (peak loads at failure) and indenter displacements at failure for the six two-flat bar-stiffened specimen simulation cases listed in Table 11. The indenter displacement data omits the small indenter traversal distance prior to specimen plate contact.

Table 14. Comparison of LS-DYNA Computed Failure Conditions with NTNU Test Data for Flat Bar-Stiffened Panel 2-FB

LS-DYNA Run ID	Mesh	MAT224 Failure Option	Maximum Contact Force (kN)	Indenter Displacement at Peak Force (mm)
1592004	1 (coarse)	*failopt* 0	1425.3	163.8
1592005	2 (medium)	*failopt* 0	1263.8	151.2
1592006	3 (fine)	*failopt* 0	1148.0	137.3
1592007	1 (coarse)	*failopt* 1	1382.4	158.5
1592009	2 (medium)	*failopt* 1	1230.2	145.7
1592010	3 (fine)	*failopt* 1	1110.2	134.2
Experimental Data			1079	139.8

Figure 21 compares LS-DYNA-computed indenter force versus displacement curves for the single flat bar-stiffened panel specimen with NTNU-measured data. For this specimen, failure was anticipated in the vicinity of the 130 mm loading machine reset point accepted for the previous specimens, so reset was performed at a lower displacement to avoid failure process interference. The computed trends are quantitatively correct, and unlike the unstiffened and single flat bar-stiffened specimens, computed failure loads show clear convergence toward experimental failure load as element sizes decrease. In addition, *failopt* choice has relatively little influence.

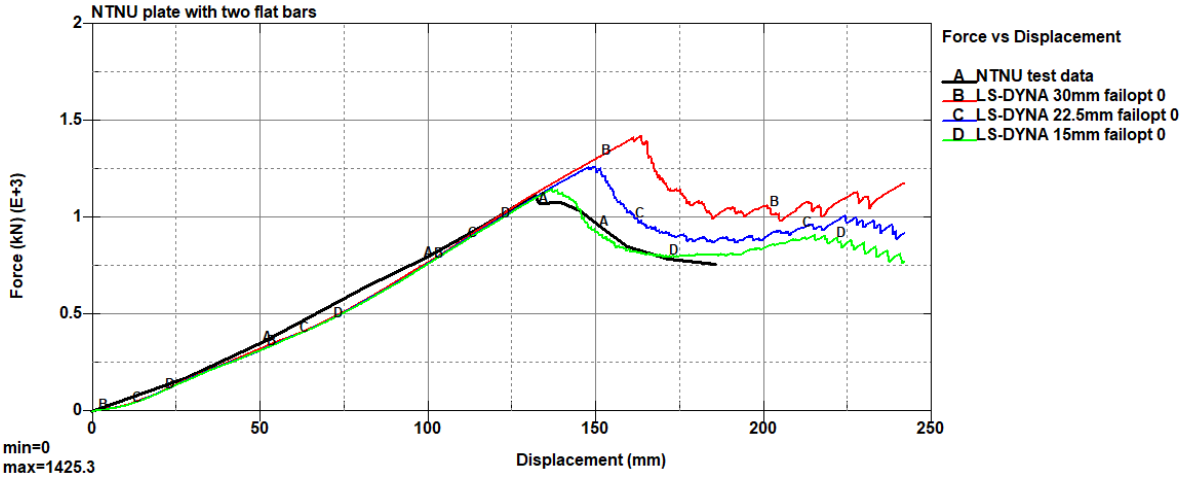

(a) *Failopt* = 0

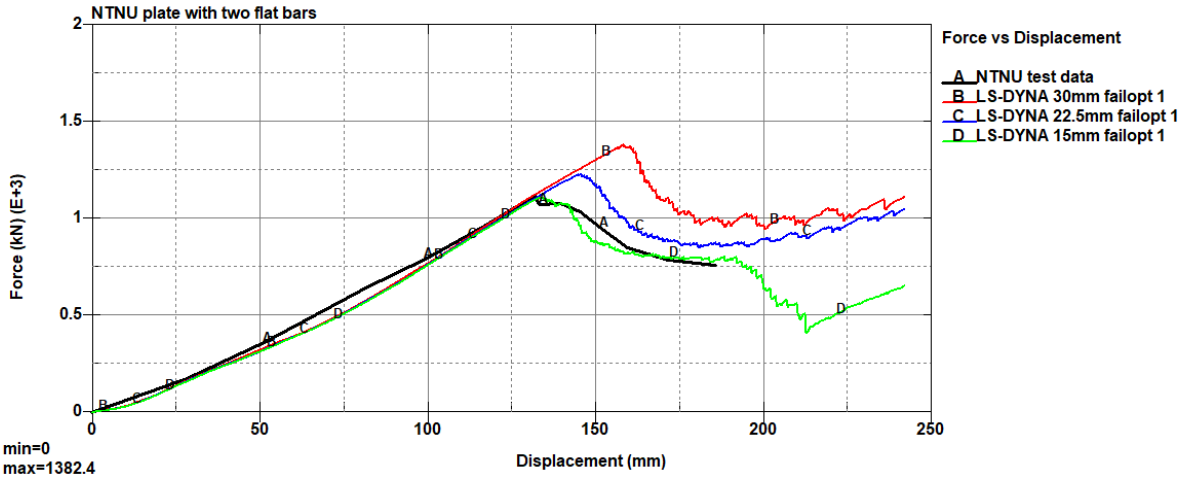

(b) *Failopt* = 1

Figure 21. Comparison of LS-DYNA-Computed Indenter Force versus Displacement Curves with NTNU Test Data for FB-2 Panels

Figure 22 additionally interprets the results pictured in Figure 21. In this figure, peak load is plotted as a function of LS-DYNA shell element *l/t* ratio with separate curves for the two MAT224 failure condition definition options. Peak load as a function of *l/t* is also plotted for the LS-DYNA and ABAQUS analyses documented by Alsos, Amdahl, and Hopperstad (2009) and AbuBakar and Dow (2013), respectively.

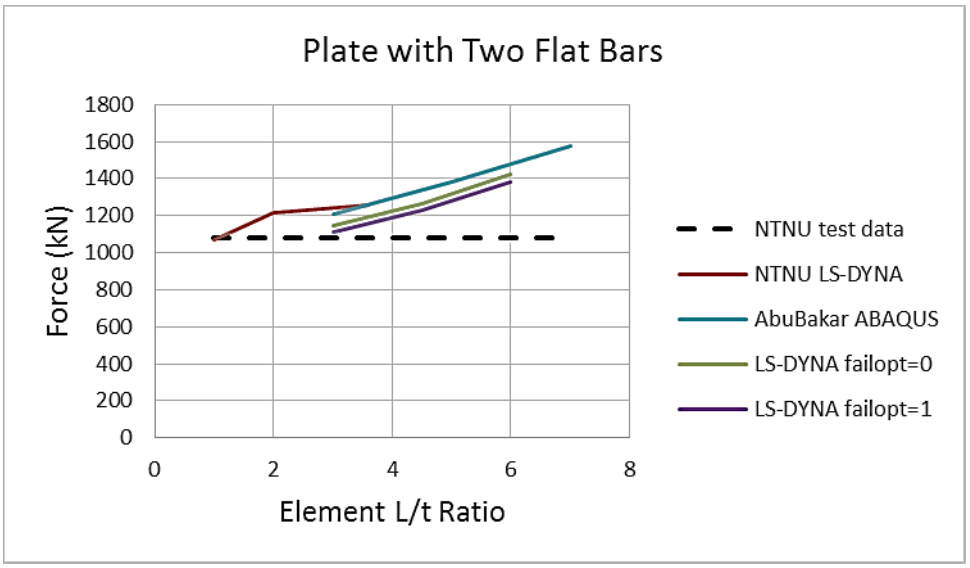

Figure 22. FB-2 Panel Peak Load versus Element Size Ratio

Figure 22 indicates a trend for all computed failure loads, from both the present work and previous work, to approach the measured failure load with increasing mesh density. The present LS-DYNA simulation results agree better with experiment than those of the prior investigators, and the difference between failure loads between the two LS-DYNA MAT224 *failopt* approaches is minor.

For the FB-2 specimen, the experimental outcome was a single slightly-curved tear close to the inboard side of one of the two plate/flat bar welded joints. Figure 23 illustrates LS-DYNA-computed crack patterns from the first few full-model binary database data-writing steps after the start of element failure for the *failopt = 0* option. Single linear tears develop for all three meshes, with short cracks developing perpendicular to the original crack at later times for the medium and fine meshes. The initial straight crack might have become curved in the manner of the test article crack if the FE mesh had been crack path-objective rather than being constrained by rectangular elements.

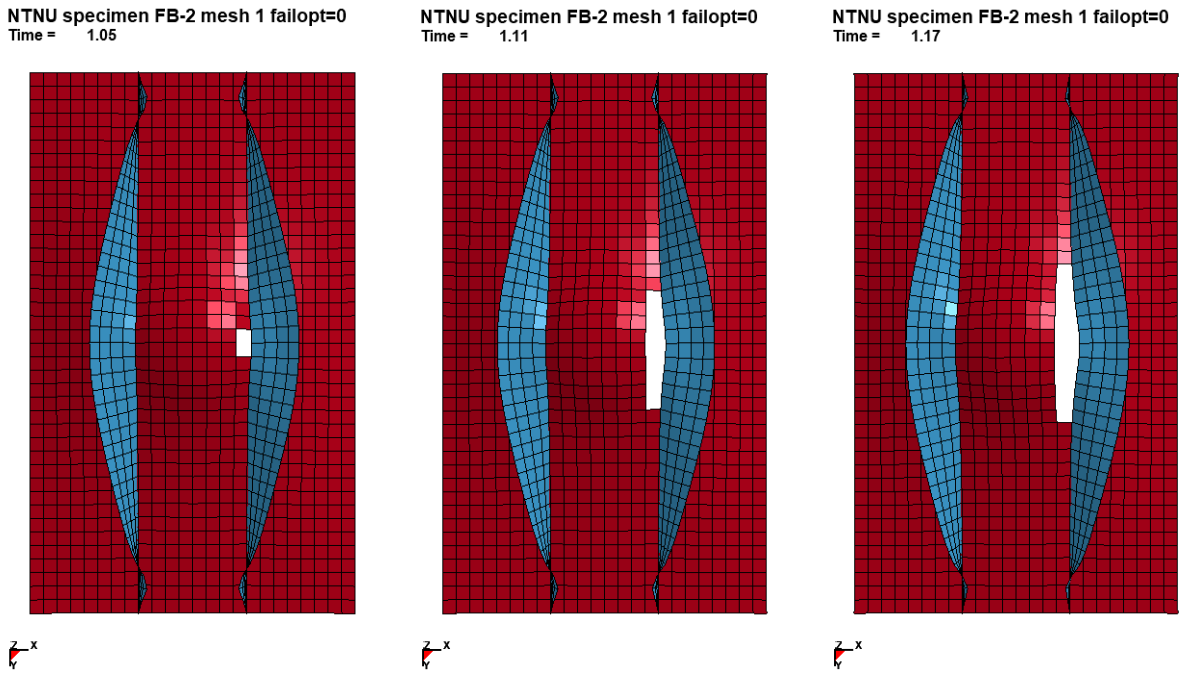

(a) *l/t* = 6

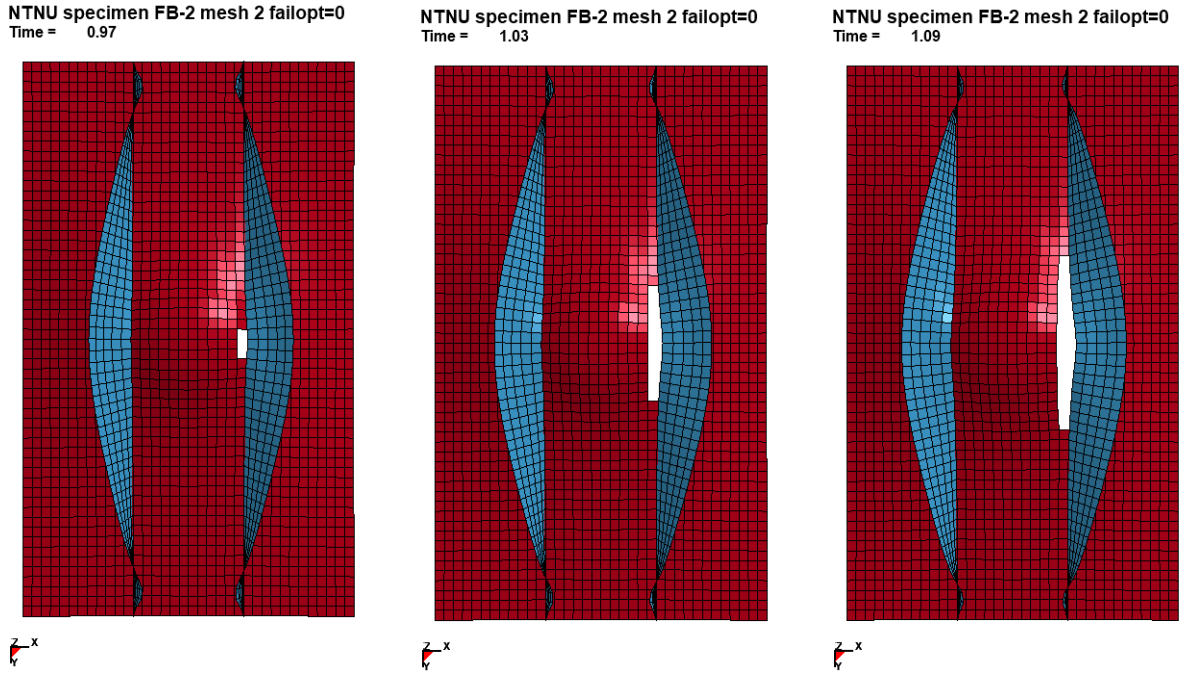

(b) *l/t* = 4.5

Figure 23. LS-DYNA-Computed Tearing Patterns in FB-2, *failopt* = 0

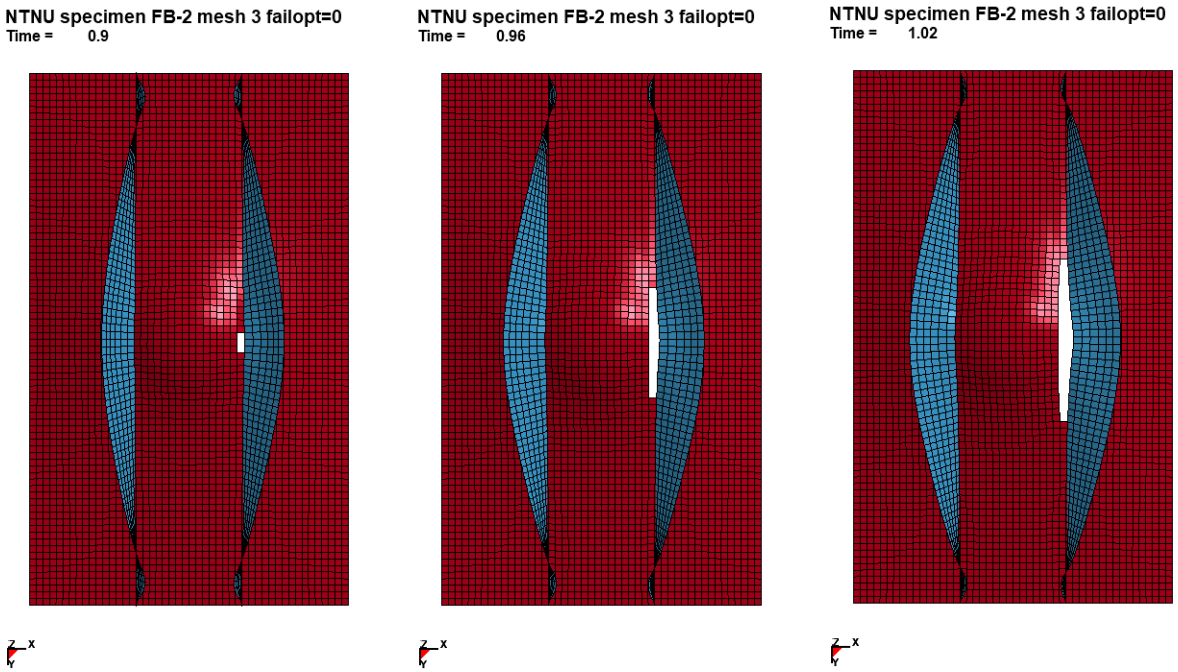

(c) *l/t* = 3

Figure 23. LS-DYNA-Computed Tearing Patterns in FB-2, *failopt* = 0 (cont'd)

Figure 24 provides similar data for the *failopt = 1* option. The simple one-crack patterns for the coarse and medium meshes agree with those obtained with *failopt = 0*. However, for the finest mesh, a second crack develops on the inboard side of the second stiffener and the two cracks eventually merge into a U shape.

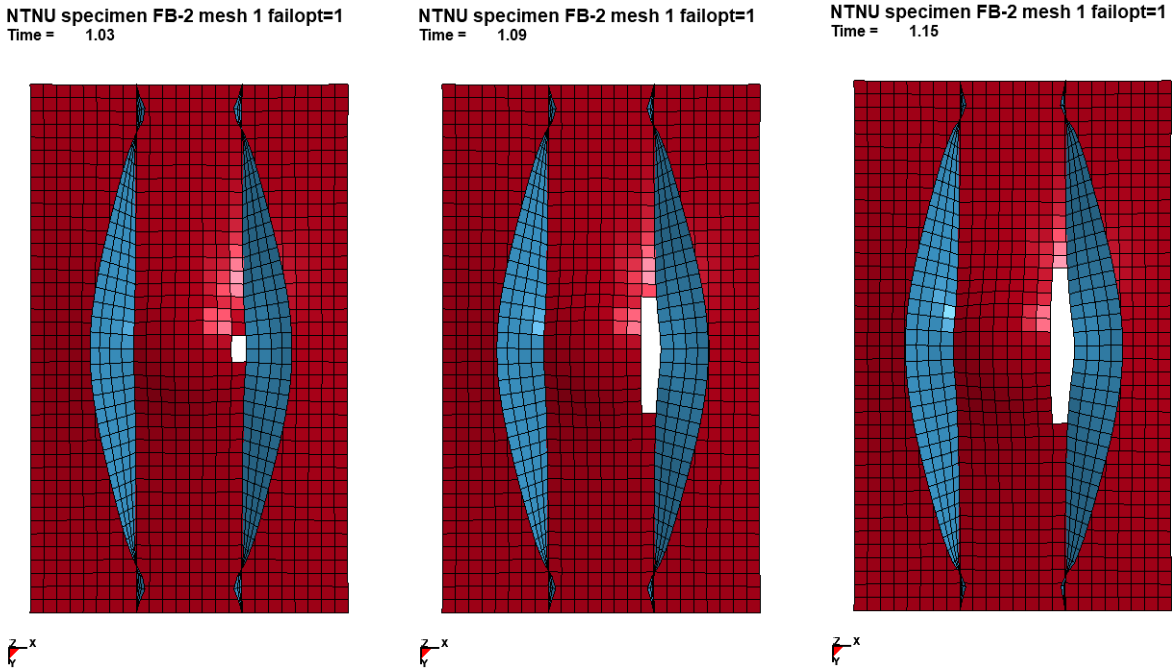

(a) *l/t* = 6

Figure 24. LS-DYNA-Computed Tearing Patterns in FB-2, *failopt* = 1

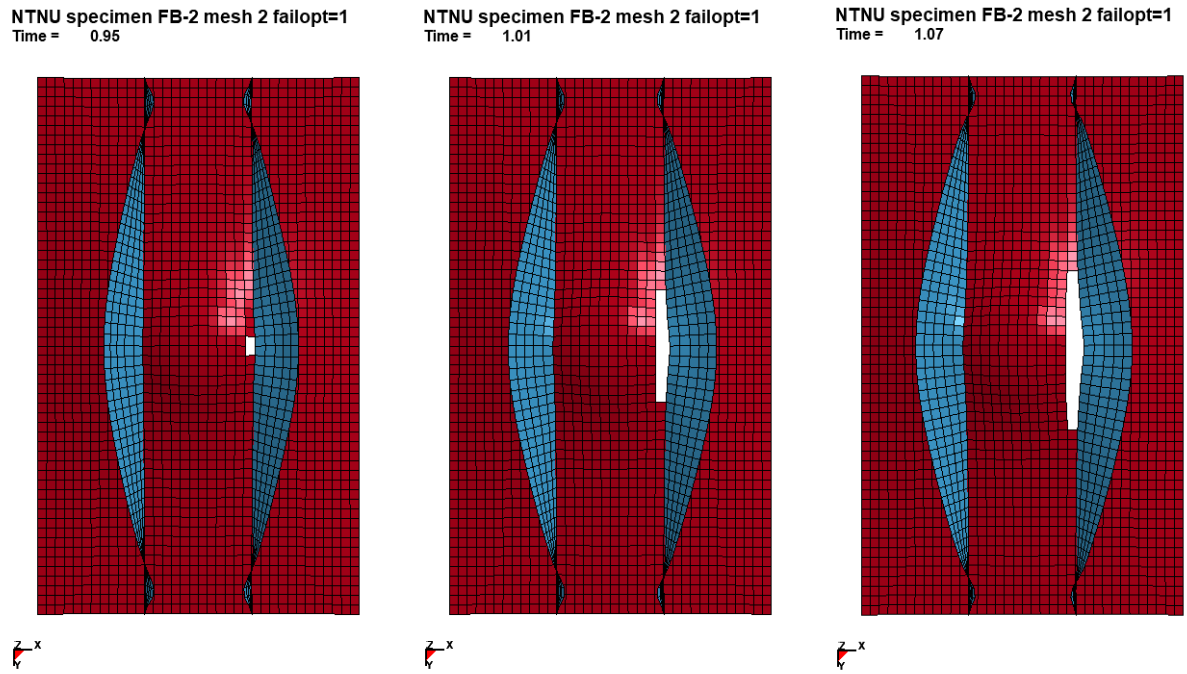

(b) *l/t* = 4.5

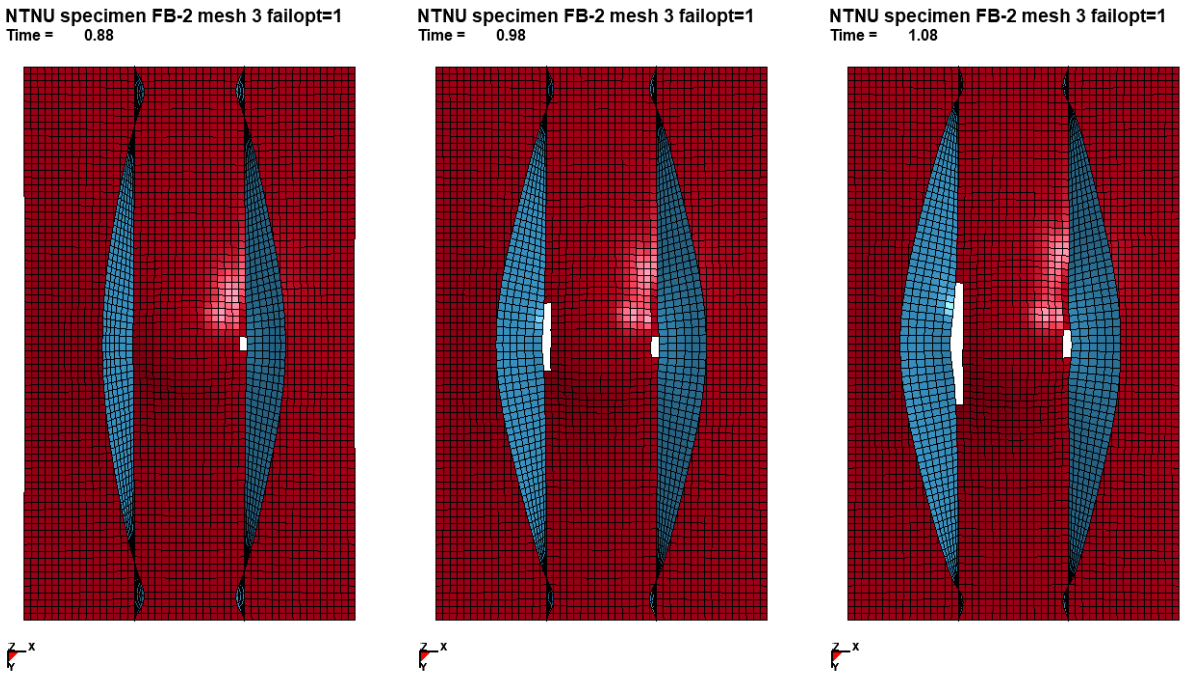

(c) *l/t* = 3

Figure 24. LS-DYNA-Computed Tearing Patterns in FB-2, *failopt* = 1 (cont'd)

For the plate stiffened by two flat bars with the plating between the flat bars directly loaded, it is clear that mesh density improves the quality of failure process prediction. In the FB-2 case, the path-dependent *failopt = 0* provided good failure load and crack pattern accuracy while the path-independent *failopt = 1* option yielded a more conservative peak load prediction, indicating somewhat "weaker" fracture resistance.

In summary, the favorable comparisons of rupture load and tearing damage predictions provided by LS-DYNA simulations for three thin plate test articles indenter-loaded in tests conducted by NTNU validates the usage of LS-DYNA MAT224 and the H-SR failure criterion for the modeling of rupture and tearing damage in thin plating composed of ductile steels. However, the most accurate and conservative predictions tended to follow from models with meshes featuring element length to thickness ratios *(l/t*) at 4.5 and below. This is a cautionary note concerning usage of meshes with *l/t* in the 5.0 to 6.0 range. Nevertheless, computations with models possessing elements in the higher *l/t* regime should still provide useful engineering information. The tearing damage predictions point toward the strain path-dependent *failopt = 0* MAT224 option as being more accurate with respect to measured crack pattern outcomes, although the path-independent option *failopt = 1* provides lower and more conservative failure loads with greater tearing damage, consistent with prior stiffened panel simulations not correlated with any experiments (Lesar, 2020).

5. Conclusions

The LS-DYNA simulations of the NTNU-conducted tests described in this report demonstrate the validity of using the HSR criterion with Lode angle independence to define a stress state-dependent failure strain curve in FE simulations of the rupture and tearing of thin-walled ship-like structures subjected to severe indentation loads. Credible predictions of rupture failure are produced in LS-DYNA simulations of laboratory experiments of the punching of unstiffened and bar-stiffened steel panels. The FE meshes employed contain elements of length-to-thickness ratios that are practical to use in analyses of large ship structures. At the same time, this study indicates the need for careful FEM design to minimize mesh-dependence, especially if fracture initiates in way of a high stress gradient.

The loading rates employed in the laboratory tests utilized here are relatively slow, and are confined to "punching" action with no "raking" movement of indenter on the structure. The performance of structural damage modeling methods for more dynamic loadings that include more complex relative movements of indenter and target structure is of high interest. The experimental "grounding test" dataset for ship-like structure acquired by NSWCCD in the 1990s (Rodd and Sikora, 1995) that resulted in significant hull plate rupture and tearing is a natural LS-DYNA numerical simulation resource. At the time of this report, LS-DYNA modeling efforts of the Rodd and Sikora grounding tests are underway at Memorial University[4], and the results of this effort will, in time, be made available to the U.S. Navy (USN) as an addition to the ship structural damage modeling methods validation body of knowledge useful for the ice impact technical area.

[4] Private communication from Professor Bruce Quinton, Memorial University.

6. Recommendations

The work reported here utilized available dry-land laboratory experimental data in attempts to validate techniques for numerical modeling of floating ice/naval surface ship collision events. These tests addressed one piece of the overall interaction problem; the numerical modeling of puncture and tearing of ship-like structures under intense local loads. To the author's knowledge, no physical tests thus far completed or under way allow ice impact and sustained sliding loading severe enough to cause rupture and tearing of the structure. If the establishment of naval ship operational limits based on hull rupture and tearing damage risk is deemed of critical importance, then experiments subjecting hull structure to ice loading severe enough to initiate rupture are necessary to help validate simulations that include ice compliance and the possibility of ice failures significant enough to effect collision loading.

The author recommends development of capabilities to conduct laboratory experiments of ship structure/ice body collisions of the scale required to provide experimental data necessary to validate numerical modeling and simulation methods for predicting structural rupture and tearing damage due to ice impact. Given the high ductility of naval ship structural steels, the energies and colliding body masses required to inflict such severe damage are very high; test article scale will have to be large and facilities will be costly. Nevertheless, at the time of this report, plans are in place to construct such facilities at the National Research Council (NRC) of Canada (HITT, or High Impact Test Theater) and at Memorial University (HERF, or Harsh Environment Research Facility). The HITT concept utilizes an existing ice testing basin at NRC, and will enable ice/ship structure impact experiments in a fluid-interactive environment with hydrodynamic forces acting on both bodies. Such tests support validation of high-fidelity fluid-structure interaction simulation methods such as arbitrary Lagrangian-Eulerian (ALE). Studies using this advanced computational technology have already been carried out by NRC (Gagnon and Wang, 2012; Gagnon et al., 2020). Alternatively, an LS-DYNA-implemented method using rigid body approximations for the majority of the ship modeling burden with accompanying hydrodynamic interaction approximations (MCOL) is available (Donner, Besnier, & Le Sourne, 2001; Le Sourne et al., 2003). This modeling framework, originally developed for simulation of ship/submarine or ship/ship collisions, is, with appropriately calibrated inputs, adaptable to ship/floating ice body collision scenarios. The HERF laboratory at MUN will possess a dynamic loading frame ("roller coaster") that can impart sliding loads on large-scale test articles in a manner that is not possible with the existing Large Pendulum Apparatus. This facility offers the opportunity to test structures suffering damage inflicted by ice bodies loading the structure by sustained scoring action.

Developing high-fidelity modeling of complex ice/structure impact and damage phenomena is difficult but ultimately useful. The efforts documented in this report and others referenced are gradually establishing better guidelines for modeling relevant phenomena in high-fidelity ice/structure collision simulations. These simulations require development and execution by "experts" and will not devolve to quick black-box-level tool executions in the immediate future. Nevertheless, painstaking research in developing and validating high-fidelity methods reveals phenomena that must be accounted for in lower-fidelity methods and suggests simplifying approximations for improving lower-fidelity tools that are rapidly applicable to operational-risk-evaluation questions.

7. References

AbuBakar, A. & Dow, R. S. (2013). Simulation of ship grounding damage using the finite element method. *International Journal of Solids and Structures, 50,* 623−636.

Alsos, H. S. & Amdahl, J. (2009). On the resistance to penetration of stiffened plates, part I: Experiments. *International Journal of Impact Engineering, 36,* 799−807.

Alsos, H. S., Amdahl, J., & Hopperstad, O. S. (2009). On the resistance to penetration of stiffened plates, part II: Numerical analysis. *International Journal of Impact Engineering, 36,* 875−887.

Bressan, J. D. & Williams, J. A. (1983). The use of a shear instability criterion to predict local necking in sheet metal deformation. *International Journal of Mechanical Sciences, 25,* 155−168.

Cockcroft, M. C. & Latham, D. J. (1968). Ductility and workability of metals. *Journal of the Institute of Metals, 96,* 33−39.

Das, J., Polić, D., Ehlers, S., & Amdahl, J. (2014). Numerical simulation of an ice beam in four-point bending using SPH. *American Society of Mechanical Engineers Proceedings, Volume 10: Polar and Arctic Science and Technology,* OMAE2014-23228. doi: 10.1115/OMAE2014-23228

Dolny, J., Daley, C., Quinton, B., & Daley, K. (2017). *ONR ice capability assessment and experimental planning, Deliverable #2: Advanced modeling and re-assessment of NSWCCD Hull 3000* [Technical report]. Houston, TX: American Bureau of Shipping.

Donner, R., Besnier, F., & Le Sourne, H. (2001). *Numerical simulation of ship-submarine collisions*. Paper presented at the 8th International Symposium on Practical Design of Ships and Other Floating Structures. Retreived from https://www.researchgate.net/publication/267040911

FEMAP (Version 019.1) [Computer software]. Plano, TX: Siemens Product Lifecycle Management Software, Inc.

Gagnon, R. E., & Derradji-Aouet, A. (2006). First results of numerical simulations of bergy bit collisions with the CCGS Terry Fox icebreaker. In H. Saeki (Ed.), *Proceedings of the 18th IAHR International Symposium on Ice* (pp. 9–16). Sapporo, Hokkaido, Japan: Hokkaido University.

Gagnon, R. E., & Wang, J. (2012). Numerical simulations of a tanker collision with a bergy bit incorporating hydrodynamics, a validated ice model, and damage to the vessel. *Cold Regions Science and Technology, 81,* 26–35.

Gagnon, R. E., Wang, J., Seo, D., & Mackay, J. (2020). Numerical simulations of naval vessel collisions with ice. Manuscript submitted for publication/presentation at IAHR 2020 Ice Symposium, Trondheim, Norway, November, 2020.

Hill, R. (1952). On discontinuous plastic states with reference to localized necking in thin sheets. *Journal of Mechanics and Physics of Solids, 1*(1), 19−30.

Kim, E., Storheim, M., Amdahl, J., Løset, S., & von Bock und Polach, R. U. F. (2016). Laboratory experiments on shared-energy collisions between freshwater ice blocks and a floating steel structure. *Journal of Ships and Offshore Structures, 12*(4), 530–544. doi: 10.1080/17445302.2016.1183270

Kim, H. (2014). *Simulation of compressive cone-shaped ice specimen experiments using LS-DYNA.* Paper presented at the 13th International LS-DYNA User's Conference, Detroit, MI. Retrieved from https://www.dynalook.com/conferences/13th-international-ls-dyna-conference/constitutive-modeling/simulation-of-compressive-2018cone-shaped2019-ice-specimen-experiments-using-ls-dyna-r

Lesar, D. E. (2017). *Modeling and simulation of ice failure modes during ice floe / ship structure collision* (NSWCCD-65-TR–2017/12). West Bethesda, MD: Naval Surface Warfare Center, Carderock Division.

Lesar, D. E. (2019). *Modeling and simulation of ice floe/ship structure collision with inelastic structural deformation, ice crushing, and ice flexural fracture* (NSWCCD-65-TR–2018/13). West Bethesda, MD: Naval Surface Warfare Center, Carderock Division.

Lesar, D. E. (2020). *Modeling and simulation of ice body/ship structure collision with inelastic structural deformation including rupture and tearing* (NSWCCD-65-TR–2019/08). West Bethesda, MD: Naval Surface Warfare Center, Carderock Division.

Le Sourne, H., Couty, N., Besnier, F., Kammerer, C., & Lagavre, H. (2003). *LS-DYNA applications in shipbuilding*. Paper presented at the 4th European LS-DYNA User's Conference, Ulm, Germany. Retrieved from https://www.dynalook.com/conferences /european-conf-2003/ls-dyna-applications-in-shipbuilding.pdf

Liu, Z., Amdahl, J., & Løset, S. (2011). Integrated numerical analysis of an iceberg collision with a foreship structure. *Marine Structures, 24*, 377–395.

Livermore Software Technology Corporation. (2017). *LS-DYNA® keyword user's manual* (Vol. I and Vol. II, LS-DYNA R10.0, r:9023). Livermore, CA: Author.

Nahshon, K., & Miraglia, M. (2011). *An element size informed correction criteria for modeling fracture in shell elements.* Presented at the 11th U.S. National Congress on Computational Mechanics, Minneapolis, MN.

Rice, J. & Tracey, D. (1969). On the ductile enlargement of voids in triaxial stress fields. *Journal of the Mechanics and Physics of Solids, 17*(3), 201−217.

Rodd, J. L. & Sikora, J. P. (1995). Double hull grounding experiments. In *Proceedings of the Fifth (1995) IAHR International Offshore and Polar Engineering Conference* (pp. 446–456). The Hague, Netherlands.

Sazidy, M. S. (2015). *Development of velocity dependent ice flexural failure model and application to safe speed methodology for polar ships* (Doctoral dissertation). Memorial University of Newfoundland, St. John's, Newfoundland, Canada.

Stören, S. & Rice, J. R. (1975). Localized necking in thin sheets. *Journal of the Mechanics and Physics of Solids, 23*(6), 421–441.

Xue, L. (2007). Damage accumulation and fracture initiation in uncracked ductile solids, subject to triaxial loading. *International Journal of Solids and Structures, 44(16)*, 5163–5181.

Xue, L., & Wierzbicki, T. (2006). *Verification of a new fracture criterion using LS-DYNA.* Paper presented at the 9th International LS-DYNA User's Conference, Detroit, MI. Retrieved from https://www.dynalook.com/conferences/international-conf-2006 /32SimulationTechnology.pdf

This page intentionally left blank.

Appendix
Development of DH36 Steel Failure-Strain Curve as a Function of Stress Triaxiality for Plane-Stress Conditions

Development of the DH36 steel effective-plastic-failure-strain curve used in the rupture and tearing simulations reported previously (Lesar, 2020) followed the procedure outlined by Li et al. (2010). This procedure uses one of several available forming limit diagram (FLD) creation approaches, the Hill, Stören, and Rice (H-SR) method (Hill, 1952; Stören & Rice, 1975). This method defines stress-state-dependent thresholds for necking instability of thin ductile metal sheets, conservatively treated as the onset point for fracture. The H-SR criterion is not accurate for shear-dominated stress states at low triaxialities, but it is sufficiently representative for tension-dominated states where plane-stress conditions prevail.

The first step of the H-SR method is to develop a power-law curve fit to a stress-strain curve acquired in uniaxial tension tests. Upper- and lower-bound true-stress-versus-true-effective-plastic-strain curves for DH36 steel, based on measurements (Nasser & Guo, 2003) at strain rates of 1.0 s^{-1} and 0.001 s^{-1}, respectively, appear in Figure A1[5]. Curve coordinates at effective strains less than 0.159 are obtained from measured data, while coordinates above that are obtained from Johnson-Cook curve fitting. The power-law approximations of these composite measured/Johnson-Cook curves take the form

$$\sigma = K\varepsilon^N, \tag{A1}$$

where σ is effective stress, ε is effective plastic strain, and K and N are constants.

The parameters for the 1.0 s^{-1} and 0.001 s^{-1} curves are (K, N) = (1010, 0.16) and (K, N) = (855, 0.16), respectively. The power-law curves for both rates also appear in Figure A1. It is essential that they accurately represent measured data in the effective strain range where necking occurs: 0.1 to 0.3 in this case. The H-SR FLD used in the report main body follows from the nearly static lower-rate power-law curve, typified by (K, N) = (855, 0.16).

[5] These data are consistent with a quasi-static tensile test true stress vs. logarithmic strain curve for DH36 steel plate, later obtained independently (Gao, Zhang, & Roe, 2009). When elastic strain is subtracted, their quasi-static data lies between the upper and lower bounds shown in Figure A1.

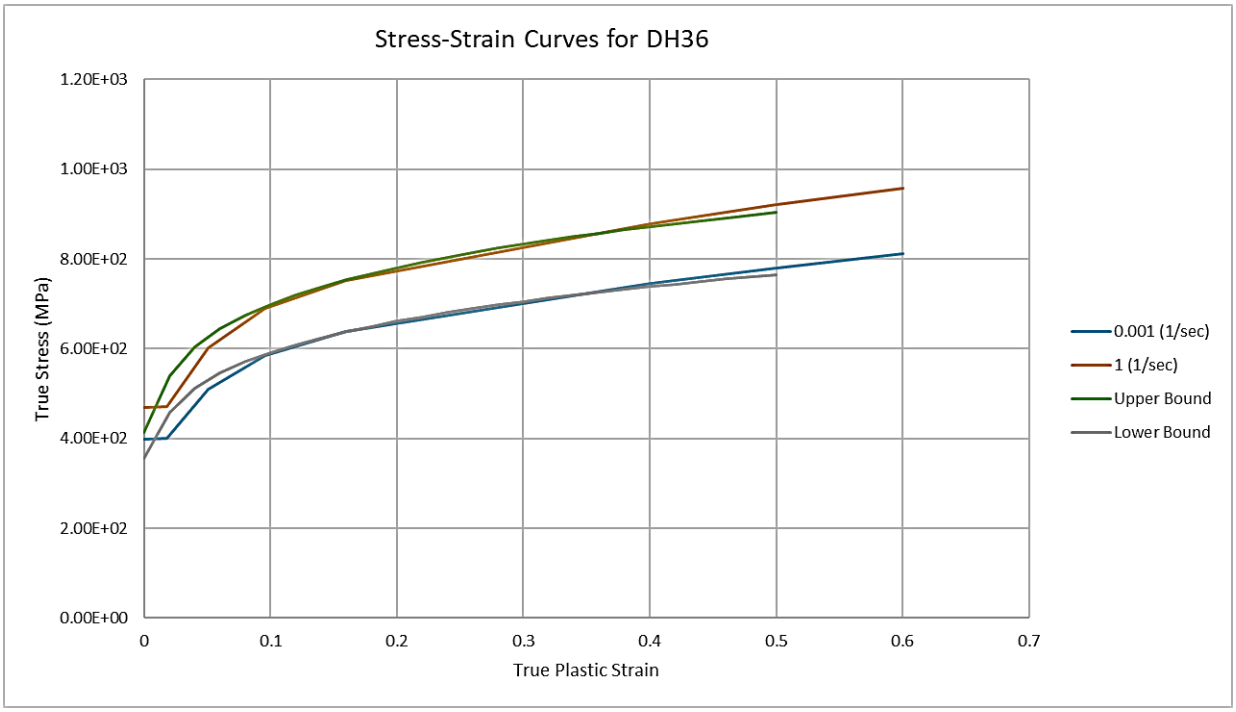

Figure A1. True-Stress-versus-True-Strain Curves for DH36 Steel for Two Strain Rates

According to the H-SR criterion, the equations for major strain at necking localization as a function of minor/major strain ratio, β, are

$$\varepsilon_1^{H-SR} = \frac{N}{1+\beta} \text{ for } -1 < \beta \leq 0 \tag{A2}$$

and

$$\varepsilon_1^{H-SR} = \frac{3\beta^2+N(2+\beta)^2}{2(2+\beta)(1+\beta+\beta^2)} \text{ for } 0 \leq \beta \leq 1, \tag{A3}$$

where $\beta = \frac{\varepsilon_2}{\varepsilon_1}$, ε_2 is minor strain, and ε_1 is major strain.

Figure A2 plots major strains at failure versus minor strains over the strain ratio range $-1 < \beta \leq 1$. Equations (2) and (3) are functions of the hardening exponent N, and the minimum failure strain value is $N = 0.16$ at $\beta = 0.0$, a condition of plane-strain tension. Since $N = 0.16$ for both bounding power-law curves, failure strain is, in this case, independent of underlying strain rate.

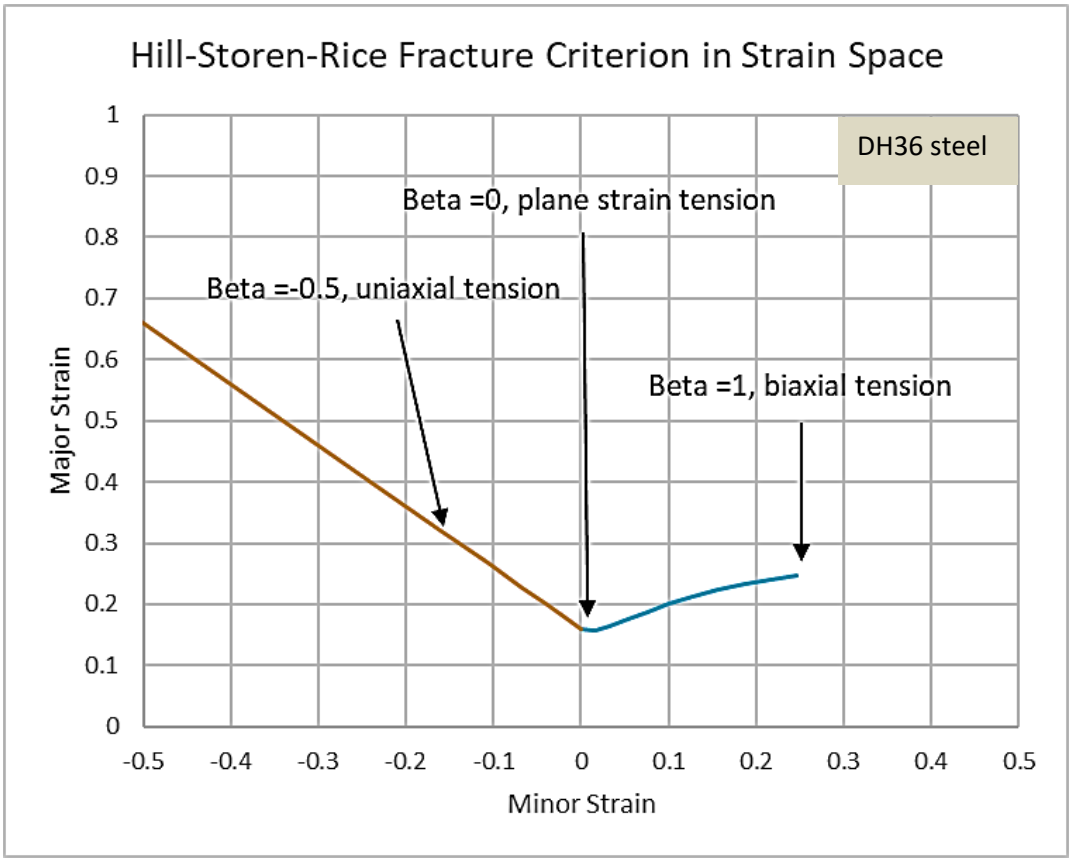

Figure A2. Major Strain at Failure versus Minor Strain, DH36 Steel

The strain-ratio-based failure curve of Figure A2 is transformable to an equivalent curve in stress space by presuming plane-stress conditions and isotropic power-law hardening (Li, Luo, Gerlach, & Wierzbicki, 2010). Equations for (1) stress triaxiality and (2) effective plastic failure strain as functions of strain ratio, β, define the failure curve in stress space.

According to Li et al., the stress triaxiality, *T* (ratio of mean stress or pressure to effective stress), as a function of strain ratio is:

$$T = \frac{1+\beta}{\sqrt{3(1+\beta+\beta^2)}}. \tag{A4}$$

The effective failure strain, also a function of strain ratio, is:

$$\varepsilon_{eff}^{H-SR} = \frac{2\sqrt{1+\beta+\beta^2}}{\sqrt{3}}\varepsilon_1^{H-SR}. \tag{A5}$$

These equations are cross-plotted in Figure A3. This is the stress-triaxiality-dependent failure-strain-curve input to LS-DYNA for MAT224 but with a change of sign in stress triaxiality to accommodate that model's unusual sign convention.

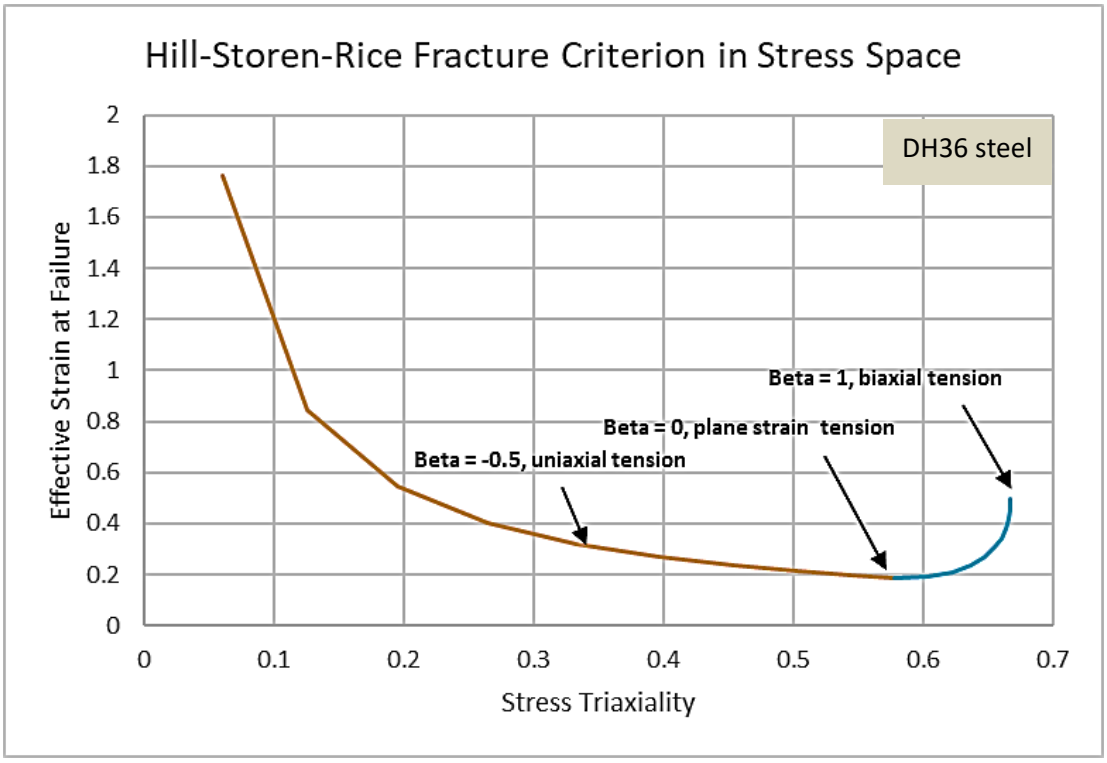

Figure A3. Effective Plastic Failure Strain versus Stress Triaxiality, DH36 Steel

A key feature of the failure strain curve in Figure A3 is the highly nonlinear portion for stress triaxialities between states of plane strain and biaxial tension (Beta = 0 and 1, respectively). A small change in triaxiality from the biaxial tension state reduces failure strain considerably from expectations based on a precise state of biaxial tension. This sensitivity must be kept in mind when relating effective plastic strain and stress triaxiality contours to occurrences of failure obtained from numerical structural dynamic simulations.

As a concluding remark, it must be noted that the approach described here for defining a stress state-dependent failure strain curve is based on a stress state instability limit, not on the onset of material fracture. This approach is conservative for usage in FE models (FEMs) of large structures composed of shell elements deforming in a state of plane stress. Highly resolved FEMs composed of 3D solid elements are required to capture the stress state developing in the localized neck that forms when material instability begins, ultimately reaching fracture across the neck. Such detailed models are impractical in simulations concerning large stiffened plate structures. For these reasons, failure strain versus stress triaxiality curves based on 3D solid element FEMs and test data for a variety of specimens tested to fracture will show much higher effective plastic strains at failure (e.g. Gao, Zhang, & Roe, 2009).

References

Hill, R. (1952). On discontinuous plastic states, with special reference to localized necking in thin sheets. *Journal of the Mechanics and Physics of Solids, 1*(1), 19–30.

Gao, X., Zhang, G., & Roe, C. (2009). A study on the effect of stress state on ductile fracture. *International Journal of Damage Mechanics*. doi:10.1177/1056789509101917.

Lesar, D. E. (2020). *Modeling and simulation of ice body/ship structure collision with inelastic structural deformation including rupture and tearing* (NSWCCD-65-TR–2019/08). West Bethesda, MD: Naval Surface Warfare Center, Carderock Division.

Li, Y., Luo, M., Gerlach, J., & Wierzbicki, T. (2010). Prediction of shear-induced fracture in sheet metal forming. *Journal of Materials Processing Technology*, *210*(14), 1858–1869.

Nasser, S. N., & Guo, W. G. (2003). Thermomechanical reponse of DH-36 structural steel over a wide range of strain rates and temperatures. *Mechanics of Materials, 35,* 1023−1047.

Stören, S. & Rice, J. R. (1975). Localized necking in thin sheets. *Journal of the Mechanics and Physics of Solids, 23*(6), 421–441.

This page intentionally left blank.


NAVSEA
CARDEROCK
Surface Warfare Center Division